A statistical study of the force balance and structure in the flux ropes in Mercury's magnetotail

J. T. Zhao,[1] W. J. Sun,[2] Q. G. Zong,[1] J. A. Slavin,[2] X. Z. Zhou,[1] R. M. Dewey,[2] G. K. Poh,[3,4], and J. M. Raines[2]

Corresponding author: Q. G. Zong, (qgzong@pku.edu.cn) and W. J. Sun, (wjsun@umich.edu).

[1]School of Earth and Space Sciences, Peking University, Beijing 100871, China.

[2]Department of Climate and Space Sciences and Engineering, University of Michigan, Ann Arbor, Michigan 48109, USA.

[3]Solar System Exploration Division, NASA Goddard Space Flight Center, Greenbelt, Maryland 20771, USA

[4]Center for Research and Exploration in Space Sciences & Technology II, University of Maryland Baltimore County, Baltimore, Maryland 21250, USA

Abstract. This study presents a statistical investigation of the force balance and structures in the flux ropes in Mercury's magnetotail plasma sheet by using the measurements of MErcury Surface,Space ENviroment,GEochemistry,and Ranging (MESSENGER). 168 flux ropes was identified from the 14 hot seasons of MESSENGER from 11 March 2011 to 30 April 2015, and 143 of them show clear magnetic field enhancements with the core field being $\geq$ 20% higher than the background magnetic field. The investigation on the force balance of these 143 flux ropes shows that magnetic pressure gradient force cannot be solely balanced by magnetic tension force, implying that thermal plasma pressure gradient force cannot be neglected in the flux ropes. We employ a non-force-free model considering the contribution of thermal pressure to resolve the physical properties of flux ropes in Mercury's magnetotail. 28 flux ropes are obtained through the fitting to the non-force-free model. The flux ropes are found to be consistent with the flattened structures, in which the mean semi-major is $\sim$ 851 km and semi-minor is $\sim$ 333 km, both are several times the local proton inertial length. The average core field is estimated to be $\sim$ 57.5 nT and flux content is $\sim$ 0.019 MWb, much larger than the previous results obtained from force-free flux rope model. The importance of thermal pressure gradient in the force-balance of the flux ropes and the flattened structure indicate the flux ropes in Mercury's magnetotail plasma sheet are mostly in early stage of the evolution, and still contain enough plasma to affect their magnetic structures.

1. Introduction

Mercury is the innermost planet in the Solar System with an orbital period of only $\sim$ 88 Earth solar days. The Mercury's elliptical orbit about the sun has an aphelion of $\sim$ 0.47 AU (Astronomical Unit, 1 AU = 1.496×10^8 km) and a perihelion of $\sim$ 0.31 AU. The proximity of Mercury's orbit to the sun result in it experiencing interplanetary conditions much different from the other planets in the Solar System. For example, the solar wind is hotter, solar wind density is higher, and the interplanetary magnetic field (IMF) is much stronger at Mercury than those at Earth ($\sim$ 1 AU) [e.g., *Russell et al.*, 1988; *Glassmeier*, 1997; *Slavin et al.*, 2007]. Observations from Mariner 10 and MErcury Surface, Space ENviroment, GEochemistry, and Ranging (MESSENGER) [*Solomon et al.*, 2001] have revealed that Mercury's internal magnetic field is closely aligned ($< 5°$) with the planet's rotation axis, and has the same polarity as the Earth. However, the magnetic field near Mercury's surface is only $\sim$ 1% of Earth's surface field [e.g., *Ness et al.*, 1976; *Alexeev et al.*, 2010; *Anderson et al.*, 2010, 2011]. Due to the higher solar wind pressure, weaker internal magnetic field, and stronger dayside magnetopause erosion [e.g., *Slavin and Holzer*, 1979], the subsolar standoff distance for Mercury's magnetopause is only $\sim$ 0.45 R_M, where $R_M \sim$ 2440 km is Mercury's radius, above the surface of the planet [e.g., *Winslow et al.*, 2013; *Zhong et al.*, 2015]. As a result, Mercury itself occupies a much larger fraction of the magnetosphere than Earth, Saturn, and Jupiter [e.g., *Jackman et al.*, 2014].

Mercury's magnetosphere experiences many processes and structures closely related with magnetic reconnection similar to the Earth's magnetosphere, such as the flux transfer events (FTEs) near the dayside magnetopause [e.g., *Russell and Walker*, 1985; *Slavin et al.*, 2012a], flux ropes and travelling compression regions (TCRs) in the magnetotail [*Slavin et al.*, 2009, 2012b; *DiBraccio et al.*, 2015; *Sun et al.*, 2016; *Smith et al.*, 2017; *Zhong et al.*, 2018], and dipolarizations [*Sun et al.*, 2015a, b, 2017, 2018; *Dewey et al.*, 2017]. Flux ropes were proposed to be formed between the near and distant neutral lines during Earth's magnetospheric substorm with magnetic loop profiles (or "O-lines") in 1970s [*Schindler*, 1974; *Hones*, 1977]. The formation of magnetic loop topology inside flux ropes would require perfect anti-parallel magnetic field lines (180° separation angle)[*Hughes and Sibeck*, 1987; *Zong et al.*, 1997, 2004]. However, because a dawn-dusk component in the magnetotail magnetic field is common, magnetic reconnection would generate the flux ropes with helical field line topology [e.g., *Hughes and Sibeck*, 1987; *Slavin et al.*, 1989; *Hesse and Birn*, 1991; *Moldwin and Hughes*, 1991; *Zong et al.*, 1997, 2004]. A statistical survey on the spatial distribution of flux ropes in Mercury's magnetotail showed that flux ropes were more frequently observed on the dawnside plasma sheet than on the duskside [*Sun et al.*, 2016], indicating that the dawnside plasma sheet is more dynamic than the duskside plasma sheet. This feature was confirmed by the subsequent studies on dipolarizations and particle energization, including proton and electron, in the near planet region of Mercury [*Sun et al.*, 2017; *Dewey et al.*, 2017; *Smith et al.*, 2017; *Poh et al.*, 2017a].

The flux ropes could be fitted to a force-free flux rope model whose solution is Bessel functions, which give the diameter, core field intensity, and magnetic flux content for the structures [e.g., *Lundquist*, 1950; *Burlaga*, 1988; *Lepping et al.*, 1996; *Slavin et al.*, 2003]. The underlying assumptions of this force-free model include J being parallel to

B everywhere ($\vec{J} \times \vec{B} = 0$) and the flux rope being cylindrical in shape. There are also several flux rope models that consider the nature of non-force-free of flux ropes and the influence of gradients in plasma pressure. [e.g., *Moldwin and Hughes*, 1991; *Kivelson and Khurana*, 1995; *Hidalgo et al.*, 2002]. In particular, *Kivelson and Khurana* [1995] developed models for flux ropes embedded in Harris current sheet, which contain solutions for both force-free and non-force-free flux ropes. Their models have been successfully applied in the flux ropes in the Earth's plasma sheet observed during Galileo's Earth flyby [*Kivelson and Khurana*, 1995]. In addition, *Slavin et al.* [2009] and *Slavin et al.* [2012a] analyzed FTE-type flux ropes at the Mercury's magnetopause using force-free [*Lundquist*, 1950] and non-force-free [*Hidalgo et al.*, 2002] models.

By employing the force-free flux rope model first developed by *Lundquist* [1950], *DiBraccio et al.* [2015] and *Smith et al.* [2017] conducted statistical studies on the flux ropes in Mercury's magnetotail. Because MESSENGER could not directly resolve the proton bulk flow velocity, both of them assumed a velocity of ~ 465 km/s for the flux ropes, which was an average value of background Alfvén speed. The radius of flux rope was found to be ~ 200 km comparable to the background ion inertial length. The flux content of flux rope was only ~ 0.002 MWb on average, which was much smaller (by an order of magnitude) than the latterly reported average magnetic flux of dipolaring flux bundles (DFBs) following dipolarization fronts (~ 0.06 MWb) [*Dewey et al.*, 2018] and two orders of magnitude smaller than the magnetic flux loaded into Mercury's magnetotail during the substorm growth phase ($\sim$ 0.69 MWb) [*Slavin et al.*, 2010; *Imber and Slavin*, 2017].

However, the new MMS observations have shown that thermal pressure gradients are important in newly formed ion-scale flux ropes [*Farrugia et al.*, 2016; *Zhao et al.*, 2016].

Because the flux ropes at Mercury are ion-scale, and may have formed only recently, its force balance within the flux ropes in Mercury's tail may also involve significant plasma pressure gradients. Since force-free model does not consider the contribution of thermal pressure, if the thermal pressure is significant, thus it may be important to apply a non-force-free model to the flux ropes in Mercury's tail.

Here, we investigate the force balance within these flux ropes at Mercury, Our results show that thermal plasma pressure gradients cannot be ignored inside most of the flux ropes. The physical properties of the flux ropes are determined by comparing the results of non-force-free and force-free modeling. This study finds that most of the ion-scale flux ropes observed in Mercury's magnetotail by MESSENGER appear to have formed recently and still contain significant amounts of plasma, which might still be able to affect their magnetic structures.

This paper arranges as follows. In Section 2, the instrumentation and data will be described. In Section 3, at first, we will show a flux rope case study. Secondly, we will statistically investigate the force balance of flux ropes, and then we will describe the non-force-free flux rope model employed in this research. Section 4 will provide detail statistical results for the structure of flux ropes in Mercury's magnetotail. Discussion and Conclusions makeup the final two sections.

2. Instrumentation and Data

This study employs magnetic field and plasma measurements from MESSENGER. The magnetometer (MAG) measures magnetic field vector in a time resolution of 20 samples per second [*Anderson et al.*, 2007]. The position data of MESSENGER were provided by accompanying with the magnetic field data at the same time resolution. The Fast

Imaging Plasma Spectrometer (FIPS), which is one part of the Energetic Particle and Plasma Spectrometer (EPPS) [*Andrews et al.*, 2007], measures ions with mass - amu over an energy range from $\sim$ 46 eV/e to 13.3 keV/e in every 10 seconds. However, MESSENGER'S thermal sun shade limits its field of view to $\sim 1.4\pi$ sr. FIPS also provides one minute proton moments, which were obtained by averaging the proton spectra over one minute intervals under the assumption of isotropic and subsonic of protons [*Raines et al.*, 2011; *Gershman et al.*, 2013].

The magnetic field data is in the Mercury Solar Magnetospheric (MSM) coordinate system, in which the X_{MSM} axis is sunward, Z_{MSM} axis points northward, and Y_{MSM} axis completes the right-handed coordinate system. The center of MSM coordinate is ~ 0.196 R_M northward offset from the Mercury's solid center [*Alexeev et al.*, 2010; *Anderson et al.*, 2010, 2011]. Position data of MESSENGER in $X-Y$ plane were aberrated according to an angle between the anti-sunward solar wind and the orbital motion of Mercury around the Sun. The solar wind velocity was set to be constantly -400 km/s and orbital velocity of Mercury was daily averaged. The aberrated coordinate is labeled as MSM′ (X'_{MSM}, Y'_{MSM}, Z'_{MSM}). The position aberration will not affect Z_{MSM}.

MESSENGER entered the orbit around Mercury on 11 March 2011, and impacted the surface of Mercury on 30 April 2015. The MESSENGER orbits could be divided into 'hot' and 'warm' seasons according to the locations of the periapsides [*Slavin et al.*, 2014]. Hot seasons correspond to the orbits for which periapsis was located on the dayside and the warm seasons with them on the nightside. During the hot seasons, MESSENGER normally crossed the Mercury's magnetotail at a distance between ~ -1.8 R_M and -3 R_M, which was close to the mean near Mercury neutral line (NMNL) [*Slavin et al.*, 2012b; *Poh* *et al.*, 2017b]. This study surveys all of the hot seasons for the presence of flux ropes. Table 1 shows the start and end times for the 14 hot seasons between 23 March 2011 and 6 April 2015. The central plasma sheet was defined to by $\beta_{\mathrm{p}} > 0.5$ [*Sun et al.*, 2016], where the β_{p} is the ratio of proton thermal pressure to the magnetic pressure in the one minute data set, where the magnetic field data is averaged down to the same one minute intervals.

3. Magnetotail Flux Rope Embedded in Current Sheet

3.1. A Case of Flux Rope

A large amplitude flux rope was observed by MESSENGER between 03:12:45 and 03:12:55 UT on 17 May 2014 (Figure 1). The flux rope, marked by the shaded region, shows clearly bipolar signature in B_{z} which corresponds to peaks in B_{y} and B_{t}. At $\sim$ 03:12:49 UT, B_{y} rapidly increased from $\sim$ 30 nT to $\sim$ 94 nT in less than one second and decreased to $\sim$ 30 nT in the following second. Meanwhile, B_{z} exhibited a bipolar signature with an amplitude from peak to peak of $\sim$ 60 nT.

The magnetic field variation of this flux rope was revealed in the application of Minimum variance analysis (MVA) [*Sonnerup and Cahill*, 1967; *Sonnerup and Scheible*, 1998; *Zong et al.*, 2003]. The results show that the maximum eigenvalue is close to the intermediate eigenvalue ($\lambda_{\mathrm{max}}/\lambda_{\mathrm{int}} \sim 2$), and both of the maximum and intermediate eigenvalues are much larger than the minimum eigenvalue ($\lambda_{\mathrm{int}}/\lambda_{\mathrm{min}} \sim 48$), which are the typical results for the application of MVA on flux rope. Figures 1a and 1b show the hodograms of the magnetic field of the flux rope under local coordinate determined by MVA. One hodogram is in B_{max} - B_{int} (Figure 1a), the other is in B_{max} - B_{min} (Figure 1b). It shows that the magnetic field rotates over 180° in B_{max} - B_{int} while shows a straight line in B_{max} - B_{min}, which further confirms the magnetic field variations of this flux rope.

3.2. Selection Criteria for Flux Ropes

This study applies the criteria in *Sun et al.* [2016] to select flux ropes in the plasma sheet at Mercury. In brief summary of the criteria, i) the $\Delta B_{\mathrm{t}} > 10\ nT$ (B_{t} enhancement) and $\Delta B_{\mathrm{z}} > 15\ nT$ (B_{z} bipolar change), ii) clear B_{y} enhancement, iii) clear magnetic field rotation in the MVA hodograms, and iv) events should be located inside the plasma sheet ($\beta_{\mathrm{p}} > 0.5$). Furthermore, this study has considered the plasma sheet durations under extreme solar wind conditions and includes plasma sheet crossings of 14 hot seasons.

We obtained 168 flux ropes in the 977 plasma sheet crossings among the 14 hot seasons, in which 135 are moving planetward and the other 33 events are moving tailward. Spatial distributions of the 168 flux ropes are shown in Figure 2 as blue crosses. Red lines are the orbits of MESSENGER during the hot season from 5 November 2011 to 1 December 2011, the first hot season in Table 1. The average magnetopause and bow shock locations of Mercury's magnetosphere obtained from *Winslow et al.* [2013] are shown in blue and green lines, respectively. In statistical, the mean increment of B_{t} of the 168 flux ropes is $\sim$ 17 nT, and is $\sim$ 77% in relative amplitude ($\Delta B_{\mathrm{t}}/B_{\mathrm{t}}$). The distribution of flux ropes is skewed toward dawnside on the magnetotail, which is similar to the previous observations [*Sun et al.*, 2016; *Smith et al.*, 2017]. In this figure, 126 events were located on the dawnside ($\mathrm{Y}'_{\mathrm{MSM}} < 0$), and 42 events were on the duskside ($\mathrm{Y}'_{\mathrm{MSM}} > 0$). In the 977 plasma sheet crossings, 461 orbits were on the dawnside and 416 were on the duskside according to the intersections of orbits and magnetic equatorial plane. There was $\sim$ 10% more orbits on the dawnside than on the duskside, however, this should not account for three times difference between the numbers of flux ropes on the dawnside and on the duskside.

3.3. Force Balance of the Flux Ropes

In this section, the force balance demonstrated by the magnetohydrostatic equation of the flux ropes in Mercury's magnetotail is examined. This equation is an equilibrium between plasma thermal pressure gradient force (∇p) and Hall force ($\vec{J} \times \vec{B}$). The Hall force contains magnetic pressure gradient force ($\nabla \frac{B^2}{2\mu_0}$) and magnetic tension force ($\vec{B} \cdot \nabla \vec{B}/\mu_0$). The magnetohydrostatic equation is an equalibrium between pressure gradient and magnetic tension, hereafter, we termed it as pressure-tension equilibrium equation. Along the normal direction (N, mostly along Z_{MSM}) of the tail current sheet, the pressure-tension equilibrium equation could be written as:

$$\frac{\partial}{\partial N}(p + \frac{B^2}{2\mu_0}) = \frac{B_T}{\mu_0}\frac{\partial B_N}{\partial T} \quad (1)$$

, where B_N is the normal magnetic field component (close to B_{z}), B_T is the tangential magnetic field component (close to B_{x}), p is the plasma thermal pressure. It is difficult to make a precise evaluation of this equation with only suitable magnetic field measurements, which is the case for MESSENGER observations. However, we can approximately estimate the force balance through the parameter differences between inside and outside of flux ropes on both sides of the equation [*Paschmann et al.*, 1982]:

$$\frac{\Delta(p + \frac{B^2}{2\mu_0})}{\Delta N} = \frac{B_T}{\mu_0}\frac{(B_{N^+} - B_{N^-})}{\Delta T} \quad (2)$$

. Here $B_{N^\pm}$ are the positive and negative extreme values inside the flux rope during observation, and B_T is taken as the total field adjacent to the flux rope (which is $\sim$ 31.0 nT for the case that shown in Figure 1). ΔT and ΔN denote the scale along the tangential and normal direction, respectively. Because the proton thermal pressure moment was one-minute time resolution, which was much longer than the duration of flux ropes (several seconds), only the magnetic pressure differences were considered on the lefthand side of the equation (2). In general, since the thermal pressure in the lobe was negligible compare to that in the plasma sheet, the lack of thermal pressure term would decrease the total pressure gradient on the lefthand side in this equation. ΔN is the scale along the normal direction. Since only magnetic pressure differences were considered, an additional constraint, which is $\Delta B_{\rm t}/B_{\rm t} \geq 0.2$, is applied to further select flux ropes with clear magnetic field enhancements. A total of 143 flux ropes was remained.

The next step is to obtain the $B_{\rm Lobe}$ in equation (2), which is the lobe magnetic field magnitude adjacent to the flux rope. In the magnetotail, the lobe magnetic field magnitude may be deduced from the pressure balance between lobe and plasma sheet. However, since the time resolution of ion measurements was not high enough and there were no higher energy ion (> 13.3 keV) or low energy electron measurements, the estimation of lobe field through pressure balance was not an option for this study. Hence, we take another approach to estimate the lobe field magnitude adjacent to the flux ropes. In the studies of *Slavin et al.* [2012b] and *Poh et al.* [2017b], an exponential relationship between $\mathrm{X}'_{\rm MSM}$ and $|B_L|$ was revealed in Mercury's tail:

$$|B_L(\mathrm{X})| = A \cdot |\mathrm{X}|^{-D} + C \quad (3)$$

, where $|B_L(\mathrm{X})|$ is the lobe field magnitude, X is the $\mathrm{X}'_{\rm MSM}$, A is the scaling constant, D is the power law exponent, C is the asymptotic magnetic field. Figure 3a shows the fit of the B_{t} for the first magnetotail crossings on 17 May 2014, which includes the flux rope in Figure 1 . The B_{t} was averaged over a bin of 0.1 $\mathrm{R_M}$, which was shown as the blue dots with standard deviations as the error bars. The fitted curve consists with the dots nicely except in the shaded region ($-1.7\mathrm{R_M} < \mathrm{X'_{MSM}} < -2.0\mathrm{R_M}$), which are the measurements in the plasma sheet. The B_L obtained through the fitted curve at the location of flux rope was deemed to be the B_T for the flux rope.

After utilizing the above procedures, the distribution of magnetic pressure differences and tension forces for the 143 flux ropes is shown in Figure 3b. The x axis indicates the difference of maximum magnetic field pressure inside flux ropes ($B^2_{\mathrm{core}}/2\mu_0$) and the corresponding lobe pressure ($B^2_{\mathrm{Lobe}}/2\mu_0$) for each flux rope, which is magnetic pressure part on the lefthand side in equation (2). The y axis indicates the tension force of each flux rope, which corresponds to righthand side in equation (2). Each cross in the figure represents a flux rope case. If the flux ropes were force-free ($\vec{J}\times\vec{B} = 0$), the crosses should cluster around the dashed red line with slope of one, indicating that magnetic pressure differences and tension forces equal to each other. There is a small group of flux ropes that was close to the dashed red line, i.e., quasi-force-free. The percentage is $\sim 6\%$ if one considered the the events with differences between x and y being smaller than 0.1 to be quasi-force-free, and the percentage is $\sim 13\%$ if the differences are smaller than 0.25. The shaded region around the force-free line in Figure 3b indicates the differences of x and y being smaller than 0.25. However, most of the crosses were located on the left region of the dashed red line. Since the thermal pressure on the lefthand side of equation (2) was ignored, the horizontal shift of the crosses could suggest that the thermal pressure might play a role for the flux ropes.

The linear fit of the crosses shown as the dashed green line results in slope of 0.66 and interception on x-axis of 1.02 nPa. From equation 2, the interception indicates that the average thermal pressure difference between the flux rope and outer boundary is ~ 1.02 nPa. The slope of the dashed green line implies that the average ratio of ΔN and ΔT was ~ 0.66, indicating that the the average scale of flux ropes along the X'_{MSM} was ~ 1.5 times that along Z'_{MSM}, i.e., flux ropes were flattened in the X'_{MSM}. If thermal pressure inside the flux rope was considered, there should be a horizontal shift in the distribution. All the events should distribute around a line with the similar slope as the green line but has the interception of 0.

3.4. Models of Flux Rope Embedded in Current Sheet

The Models of flux rope embedded in current sheet applied in this study was developed by *Kivelson and Khurana* [1995], hereafter this model is referred to as KK95. This model was based on the periodic sheet pinch solution of the Ampère's law [*Schindler et al.*, 1973]. A basic assumption of this model is that magnetic field and plasma thermal pressure show no gradient along the axial direction, which is approximately along the Y'_{MSM}. The KK95 model includes a force-free model and a non-force-free model. The solution of force-free flux rope in consideration of the existence of B_{y} can be written as

$$\begin{cases} B_{\mathrm{x}} = (\frac{B_L}{\chi})\sqrt{1+\varepsilon^2}\sinh(\frac{z}{L}) \\ B_{\mathrm{y}} = (\frac{B_L}{\chi})\sqrt{1+(\frac{\chi B_{\mathrm{y}0}}{B_L})^2} \\ B_{\mathrm{z}} = \varepsilon(\frac{B_L}{\chi})\sin(\frac{x}{L}) \end{cases} \quad (4)$$

where B_L is the magnetic field strength in the lobe, L is the thickness of the tail current sheet, ε is the shape factor, $B_{\mathrm{y}0}$ is the background B_{y}, and χ is

$$\chi = \varepsilon \cos(\frac{x}{L}) + \sqrt{1+\varepsilon^2}\cosh(\frac{z}{L}) \tag{5}$$

In these equations, only ε is a free parameter, and it determines the shape of the periodic sheet pinch. The larger the value of ε, the closer the shapes of magnetic field lines are circular. The ε is obtained as a least squares fit result. However, when the thermal pressure gradient (∇p) cannot be ignored, force balance equations in $X-Z$ plane should consider the contribution from thermal pressure gradient ($\vec{J} \times \vec{B} = \nabla p$). In KK95 model, they consider the thermal pressure in the form of

$$p(x,z) = \frac{p_0}{\chi^2}(1 - \gamma\varepsilon/\chi^{\kappa-2}) \tag{6}$$

where p_0 is the thermal pressure in the center of tail current sheet, and γ and κ are parameters determining the spatial profile of the pressure. The self-consistent solution for a non-force-free flux rope, after consideration of the above thermal pressure profile is given by:

$$\begin{cases} B_{\mathrm{x}} = (\frac{B_L}{\chi})\sqrt{1+\varepsilon^2}\sinh(\frac{z}{L}) \\ B_{\mathrm{y}} = (\frac{B_L}{\chi})\sqrt{(1-\frac{2\mu_0 p_0}{{B_L}^2}) + \frac{2\mu_0 p_0 \gamma\varepsilon}{{B_L}^2\chi^{\kappa-2}} + (\frac{B_{\mathrm{y}0}\chi}{B_L})^2} \\ B_{\mathrm{z}} = \varepsilon(\frac{B_L}{\chi})\sin(\frac{x}{L}) \end{cases} \tag{7}$$

In comparison with the Lundqvist solution based force-free flux rope model which solves the Bessel function [e.g., *Lundquist*, 1950; *Burlaga*, 1988; *Lepping et al.*, 1996; *Slavin et al.*, 2003], the KK95 non-force-free model takes into account not only the thermal pressure contribution, but also the boundary conditions. In this model, the variation of thermal pressure influences the spatial distribution of B_{y}, but not B_{x} and B_{z}. When ε is close to

0, equations (6) and (7) degenerate to the Harris Current Sheet (HCS) solution [*Harris*, 1962]:

$$\begin{cases} B_{\mathrm{x}} = B_L \tanh(\frac{z-z_0}{L}) \\ p = p_0 \mathrm{sech}^2(\frac{z-z_0}{L}) \end{cases} \quad (8)$$

Hence, when z is far away ($>> L$) from the center of flux rope, the magnetic field from the KK95 model is close to the values expected from the HCS model. Since the KK95 model relies on the basic parameters of the magnetotail current sheet, the thickness of the current sheet (L) for instance, we have applied HCS model into the magnetic fields during the magnetotail crossing to obtain these parameters.

Figure 4 shows the plasma sheet crossing of MESSENGER during which the flux rope in Figure 1 was observed. In Figure 4, MESSENGER travelled from the northern hemisphere ($B_{\mathrm{x}} > 0$) to the southern hemisphere ($B_{\mathrm{x}} < 0$) and crossed the plasma sheet. The flux rope was observed near the central part of the plasma sheet, which is indicated by the dashed red line. HCS fitting only employs magnetic field measurements in the southern hemisphere to mitigate the effects from dipole magnetic field, since the MESSENGER is closer to the planet in the northern hemisphere. The measured magnetic field has been transformed into the local coordinate system in the HCS fitting [*Sun et al.*, 2017; *Poh et al.*, 2017b; *Rong et al.*, 2018]. Figure 4e shows the fitting result. The black line represents the measured magnetic field, and the red line is the HCS best fit. These two are coincident indicating a very good fit. The dashed blue line shows the thermal pressure distribution in this current sheet from the HCS fitting, and the blue dots are proton thermal pressure from one minute average moments of FIPS. The blue dots are much lower than the dashed blue line, which could be due to, i) the one minute moments averaged over the peak values of thermal pressure in the central of the current sheet (especially when there were few data points inside the plasma sheet); ii) the contribution from heavy ions (mostly He^{++} for this current sheet crossing, as shown in Figure 4c, but for some crossings Na^{+} could be dominant) on the thermal pressure inside current sheet was ignored; iii) the contributions from protons with energy higher than ~ 13.3 keV (above the upper limit of FIPS) and electrons were not measured. It needs to note that the contribution from electrons to thermal pressure in Mercury's plasma sheet was calculated to be negligible compared with protons in the measurements from Mariner 10 [*Ogilvie et al.*, 1977]. The HCS fitting indicates a current sheet with a half thickness of $\sim 0.06\ \mathrm{R_M}$, which was only one-third of the average thickness of $\sim 0.18\ \mathrm{R_M}$ of Mercury's tail current sheet [*Poh et al.*, 2017b; *Rong et al.*, 2018]. The lobe field (B_L) was ~ 73 nT much stronger than the averaged lobe field (~ 50 nT) in $\mathrm{X'_{MSM}} \sim -2\ \mathrm{R_M}$ [*Poh et al.*, 2017b; *Rong et al.*, 2018]. These two features suggest that this current sheet is under strong external driving. The magnetic field fluctuations in the current sheet confirm that this plasma sheet crossing was very active. The center (z_0) of the current sheet was found to be located at $\mathrm{Z'_{MSM}} = 0.13\mathrm{R_M}$, which was close to the location of the flux rope marked by the shaded gray region (Figure 4e).

Since FIPS cannot resolve the background flow velocity for a single event due to the field of view limitation, we set the travelling speed of flux rope to be a free parameter to be determined by the best fit to the flux ropes, the Alfvén speed ($\frac{B_L}{\sqrt{\mu_0 \mathrm{n_p m_p}}}$) estimated from the B_L, the lobe magnetic field, and $\mathrm{n_p}$, proton density around flux ropes, was set as an upper limit. In the study of *DiBraccio et al.* [2015], they assumed a speed of 465 km/s for all of the flux ropes, which was obtained by averaging over the local Alfvén speeds for all adjacent plasma sheets. In this fitting, we apply $x = v(t-t_0)\cos\theta$ and $z = v(t-t_0)\sin\theta+\Delta z$ by assuming that the flux rope passed the spacecraft at a constant speed, where θ was the polar angle of flux rope's velocity in X − Z plane ($-15^\circ < \theta < 15^\circ$) given by the least squares fit, t_0 was the inflection time of B'_Z bipolar and Δz was determined by MESSENGER's position and the z_0 resulted from the HCS modelling.

The Alfvén speed ($\frac{B_L}{\sqrt{\mu_0 \mathrm{n_p m_p}}}$) for the flux rope in Figure 1 is determined to be ~ 910 km/s. Together with the parameters of current sheet, the fitting results of the flux rope were shown in Figures 1c to 1f as the dashed red lines. The similarity between observation and model fields indicates a good fitting. The fitting suggested that the flux rope had a travelling speed of ~ 900 km/s, magnetic flux content of ~ 0.010 MWb, semi-major axis (scale along $\mathrm{X'_{MSM}}$) of ~ 600 km, ε of 0.56, γ of 0.2, κ of 5. The magnetic flux content of flux rope was obtained by integrating B_y in the cross section inside the outmost field line, i.e., $\Phi = \iint B_\mathrm{y}\mathrm{d}x\mathrm{d}z$. Figure 5 shows the two-dimensional distributions of B_y and p in the plane transverse to the axis of this flux rope from the KK95 model. MESSENGER crossed close to the center axis of this flux rope. The B_y in the center was around ~ 105 nT. The distribution of p showed enhancement in the outer part, while a local minimum in the central part of the flux rope. While, the thermal pressure inside the flux rope is significantly larger than the ambient thermal pressure. The results revealed that the scale of flux rope was around twice the the scale along the x-axis from *DiBraccio et al.* [2015] and *Smith et al.* [2017] whose force free model assumes a circular cross section. The core field and magnetic flux content were also much larger than the average values from their studies. To further evaluate the result from a single case study, a statistical analysis on the flux rope properties determined using the KK95 model is presented below.

4. Statistical Results on the Flux Ropes

The 168 flux ropes were processed with the similar way as the case in previous section. The first step was to obtain the parameters of cross-tail current sheet, which contained the flux ropes, as an input of KK95 model. We picked up the fitting of cross-tail current sheet satisfying the constraint same as that in *Sun et al.* [2017], which yielded 103 qualified events. Next the flux ropes were fit to the KK95 model. The free parameters, including ε, γ, κ, and traveling speeds, were set to be varying in different range values. The magnetic field curves obtained from the model were compared with the measured magnetic fields. A least squares of minimization of the differences (χ^2) was employed to further select the events, which was similar to previous flux ropes studies [e.g., *Slavin et al.*, 2003; *DiBraccio et al.*, 2015]

$$\chi^2 = \frac{\sum_{i=1}^{N} \sum_{j=x,y,z} [(B_{jo}(i) - B_{jm}(i))/B_{to}(i)]^2}{N} \tag{9}$$

, where B_{xo}, B_{yo}, B_{zo}, and B_{to} are the components and magnitude of the measured magnetic fields, and B_{xm}, B_{ym}, and B_{zm} are the components from the KK95 model. N is the number of data points. The parameters of the model corresponding to the smallest χ^2 were output. After obtaining the χ^2 of the 103 flux ropes, a threshold of $\chi^2 < 0.1$ to further select the events results in 28 events. A different threshold of $\chi^2 < 0.05$ gives 20 events. The statistical results of the 28 and 20 flux ropes were summarized in Figure 6. The distributions from the two threshold of $\chi^2 < 0.1$ (white bars) and $\chi^2 < 0.05$ (grey bars) are similar and result in similar values. In the next paragraph, we will discuss the results from $\chi^2 < 0.1$ (white bars).

The distribution of the largest thermal pressure differences along the major axes of the flux ropes ($Z'_{MSM} = 0$) was shown in Figure 6a. The mean and median values of thermal pressure differences were ~ 1.40 nPa and ~ 1.13 nPa, respectively. The thermal pressure difference obtained through the model was larger than the average 1.02 nPa resulted in Figure 3b, which could due to the spacecraft usually not crossing the center of the flux ropes. The mean and median values of core field of flux ropes were ~ 57.5 nT and ~ 63.3 nT (Figure 6b), which was much larger than the values of 41.0 nT and 22.4 nT in *DiBraccio et al.* [2015] and *Smith et al.* [2017], respectively. Because the force free model in those studies only considered the force balance between magnetic field pressure gradient force and magnetic tension force, the decrease of thermal pressure inside the flux rope (as shown in Figure 5b), which was considered in the non-force-free model of this study, should result in the increase of magnetic field pressure and the core field in the center of flux ropes. It is found that the mean and median flux content of flux ropes is ~ 0.019 MWb and ~ 0.016 MWb, respectively ,which is around an order of magnitude higher than the ~ 0.002 MWb obtained in previous results. To further investigate the reason of the difference, we have employed the force-free model to estimate the properties for the 20 flux ropes in Figure 6. Force free results can be found in the supplementary material as Figure S1. The statistical results from force-free model give a mean flux content of ~ 0.012 MWb, which is $\sim$ 35% smaller than the value from non-force-free model. This indicates that the non-force-free model did output a relatively higher flux content for flux ropes. The mean core field is ~ 60 nT from the force-free model, which is similar to the values (~ 69.1 nT for $\chi^2 < 0.05$, ~ 57.5 nT for $\chi^2 < 0.1$.) from non-force-free model. While the radius is ~ 367 km from the force-free model, corresponding to a cross-sectional area of $\sim 5.4 \times 10^5$ km^2. The mean cross-sectional area is $\sim 9.2 \times 10^5$ km^2 for the non-force-free flux rope model. Therefore, the higher magnetic flux resulted from the non-force-free model mainly arises from the relative larger cross-sectional area.

Figure 6d shows that the semi-major of the flux ropes (along X'_{MSM}) is ~ 875 km, and Figure 6e shows that the semi-minor (along Z'_{MSM}) is ~ 356 km. On one hand, the scales are much larger than the scales in previous studies (454 km in *DiBraccio et al.* [2015] and 262 km *Smith et al.* [2017]). On the other hand, semi-major is much larger than the semi-minor indicating that flux ropes are flattened along the X'_{MSM}, which consists with the flatten conclusion reached by Figure 3b. Plasma sheet density in Mercury's magnetotail plasma sheet is found to be ~ 1 to 10 cm^{-3} [*Gershman et al.*, 2014; *Sun et al.*, 2018; *Poh et al.*, 2018], corresponding to ion inertial length of 80 to 230 km. The scales of flux ropes resulted in KK95 model are several times the ion inertial length. In Figure 3b, the ratio between of average scale of flux rope along Z'_{MSM} and X'_{MSM} was estimated to be $\sim$ 0.66. The model in this study gives a ratio of ~ 0.41. One must note that the spacecraft did not always cross the center axis of the flux rope. Hence, the scale estimated from Figure 3b might not be the real scale of the flux ropes, and this fact could be responsible to the difference between the two values. Figure 6f shows the distribution of travelling speeds of the flux ropes. As noted earlier, we have employed a different way than *DiBraccio et al.* [2015] in determining the travelling speeds of flux ropes. The mean and median speeds are ~ 560 km/s and 535 km/s, respectively, which are slightly larger than 465 km/s in *DiBraccio et al.* [2015].

5. Discussions

The distribution of flux ropes is skewed toward dawnside on Mercury's magnetotail as shown in Figure 2. This feature is similar to the previous observations [*Sun et al.*, 2016; *Smith et al.*, 2017; *Poh et al.*, 2017a] and is different from the distributions in Earth's magnetotail [e.g., *Slavin et al.*, 2005; *Imber et al.*, 2011]. In the Earth's studies, flux ropes and TCRs were more frequently observed on the duskside than on the dawnside in the near Earth neutral line region [*Slavin et al.*, 2003, 2005; *Imber et al.*, 2011]. *Slavin et al.* [2005] further showed that the flux ropes and TCRs were larger on the duskside than on the dawnside. To investigate the scale of flux ropes in Mercury's magnetotail, we have shown the distribution of the durations and amplitudes of the flux rope B_z bipolar in Figure 7. The durations and amplitudes were determined by B_z peak to peak of flux ropes. Figure 7a shows that the mean bipolar duration of flux ropes are longer on the duskside (~ 1.2 s, $0.5\mathrm{R_M}$ to $1.5\mathrm{R_M}$) than on the dawnside (~ 0.8 s), which implies that the scale in $\mathrm{X'_{MSM}}$ of flux ropes might be larger on the duskside ($\mathrm{Y'_{MSM}} > 0.5\ \mathrm{R_M}$) than on the dawnside similar to the results at Earth. We have done a two sample t-test for the events on the duskside ($\mathrm{Y'_{MSM}} > 0.5\ \mathrm{R_M}$) and dawnside ($\mathrm{Y'_{MSM}} < -0.5\ \mathrm{R_M}$). The p-value is 0.029 which is smaller than 0.05 indicating the duration difference in these two regions is credible. However, in reaching this conclusion, it assumed that travelling speed of the flux ropes were similar. For the case of Mercury's magnetotail, the magnetic field did not show much differences along the $\mathrm{Y'_{MSM}}$ in the near neutral line region [*Poh et al.*, 2017a], but the heavy ions, Na^+, was preferentially observe on the duskside [*Raines et al.*, 2013]. The average density of Na^+ was $\sim 8\%$ that of protons in Mercury's plasma sheet [*Gershman et al.*, 2014]. If we considered Na^+ in the estimation of Alfvén speed, the speed would be ∼ 40% lower on the duskside than on the dawnside, which could correspond to the duration difference of the B_z bipolar shown in Figure 7a. Therefore, the conclusion that the scales in X'_{MSM} of the flux ropes was larger on the duskside than on the dawnside might be not real. Further studies with reliable plasma flow measurements will be desirable.

Figure 7b shows the distribution of the amplitudes of B_z bipolar in the dawn-dusk direction. The amplitudes of B_z bipolar do not show clear dawn-dusk asymmetry. The amplitudes of B_z bipolar could represent the curvature radius of the flux rope magnetic field lines, and therefore, the scale of flux ropes in Z'_{MSM}. This distribution indicates that the scales of flux ropes in Z'_{MSM} do not show clear difference in the dawn-dusk direction.

In Section 3.3, the distribution of pressure-tension balance of flux ropes in Figure 3b was interpreted that most of the flux ropes were not force free. The magnetic tension force could not be solely balanced by magnetic pressure gradient force, however, there were a small group of events (∼ 13%) which were located near the dashed red line with slope being one, i.e., quasi-force-free. It was suggested that flux ropes should evolve toward being force-free and reach the minimum-energy state, which is called the 'Taylor state', with cylindrical profile eventually [e.g., *Taylor*, 1986]. Therefore, the results from Figure 3b and Figure 6 showed that thermal pressure gradient in most of the flux ropes were significant suggesting that they have only recently formed and still contain enough plasma to affect their magnetic structure. In previous studies, a weak correlation between core field inside flux ropes and guide field B_y in the plasma sheet was revealed [*Smith et al.*, 2017; *Ding and Rong*, 2018]. Our conclusion that flux ropes were recently formed suggested that the core field of the flux ropes could be skewed towards the reconnecting field from the guide field as proposed in the simulations [e.g., *Nakamura et al.*, 2016]. This factor might explain their poor correlation between core field of flux ropes and guide field.

6. Conclusions

This study has investigated the features of flux ropes in Mercury's magnetotail plasma sheet, including the force balance and flux rope structures. The spatial distribution of flux ropes shows clearly dawn-dusk asymmetry with more events being observed on the dawnside than on the duskside, which consists with the previous results [*Sun et al.*, 2016]. An investigation on the force balance of flux ropes reveals that the magnetic pressure gradient force cannot be solely balanced by magnetic tension force in most of the flux ropes, implying the importance of thermal pressure inside the flux ropes. By employing a non-force-free flux rope model, the thermal pressure differences, core field, scales, and flux contents were investigated. The mean value of the largest thermal pressure differences along X'_{MSM} of the flux ropes was $\sim$ 1.40 nPa. The average core field was estimated to be $\sim$ 57.5 nT, and flux content was $\sim$ 0.019 MWb. The average core field corresponds to a similar value of pressure, i.e. $\sim$ 1.31 nPa, as the largest thermal pressure differences along X'_{MSM}. The flux ropes had a flattened structure with scale in the X'_{MSM} direction ($\sim$ 851 km) being larger than in the Z'_{MSM} ($\sim$ 333 km). The scales of the flux ropes were several times the background proton inertial length. Besides, the average travelling speed of flux ropes was estimated to be $\sim$ 560 km/s.

Compare with the results obtained from force-free model of flux ropes in Mercury's magnetotail [*DiBraccio et al.*, 2015; *Smith et al.*, 2017], the core field and flux content in this study were much larger than the previous results, in which the core field was $\sim$ 22 nT and flux content was $\sim$ 0.002 MWb. The scale of the flux rope in this study was much larger than the previous value (~ 262 km), but the average travelling speed was comparable (465 km/s) [*DiBraccio et al.*, 2015]. The magnetic flux contained by a flux rope in previous study was an order of magnitude smaller than the the magnetic flux carried by a DFB [*Dewey et al.*, 2018], while this study reveals that the flux content of a flux rope is about one third of the flux of a DFB. It needs to note that *Fear et al.* [2017] argued that the amount of flux reconnected in the formation of the flux ropes could be greater than the flux rope contents, which might be more directly comparable with the DFB flux.

The importance of thermal pressure gradient in the force-balance of the flux ropes and the flatten structure indicate that the flux ropes observed by MESSENGER in Mercury's tail have only recently formed. The flux ropes still contained enough plasma to affect their magnetic structures as observed in PIC simulations of flux rope formation in thin current sheets [*Chen et al.*, 2017]. The core field of the early stage flux rope could be influenced by the reconnecting magnetic field, which explained the weak correlation between core field of flux ropes and the guide field as shown in previous studies [*Smith et al.*, 2017; *Ding and Rong*, 2018].

Acknowledgments. This work is supported by the National Natural Science Foundation of China (grants 41421003, 41704163, and 41627805). The University of Michigan contributions were supported by NASA's Solar System Workings program through grant NNX15AH28G.. MESSENGER data used in this study were available from the Planetary Data System (PDS): http://pds.jpl.nasa.gov. The MESSENGER project is supported by the NASA Discovery Program under contracts NASW-00002 to the Carnegie Institution of Washington and NAS5-97271 to The Johns Hopkins University Applied Physics

Laboratory. We are grateful to MESSENGER Magnetometer and Fast Imaging Plasma Spectrometer (FIPS) for providing the data.

References

Alexeev, I. I., E. S. Belenkaya, J. A. Slavin, H. Korth, B. J. Anderson, D. N. Baker, S. A. Boardsen, C. L. Johnson, M. E. Purucker, M. Sarantos, and S. C. Solomon (2010), Mercury's magnetospheric magnetic field after the first two messenger flybys, *Icarus*, *209*(1), 23 – 39, doi:https://doi.org/10.1016/j.icarus.2010.01.024, mercury after Two MESSENGER Flybys.

Anderson, B. J., M. H. Acuña, D. A. Lohr, J. Scheifele, A. Raval, H. Korth, and J. A. Slavin (2007), The magnetometer instrument on messenger, *Space Science Reviews*, *131*(1), 417–450, doi:10.1007/s11214-007-9246-7.

Anderson, B. J., M. H. Acuña, H. Korth, J. A. Slavin, H. Uno, C. L. Johnson, M. E. Purucker, S. C. Solomon, J. M. Raines, T. H. Zurbuchen, G. Gloeckler, and R. L. McNutt (2010), The magnetic field of mercury, *Space Science Reviews*, *152*(1), 307–339, doi:10.1007/s11214-009-9544-3.

Anderson, B. J., C. L. Johnson, H. Korth, M. E. Purucker, R. M. Winslow, J. A. Slavin, S. C. Solomon, R. L. McNutt, J. M. Raines, and T. H. Zurbuchen (2011), The global magnetic field of mercury from messenger orbital observations, *Science*, *333*(6051), 1859–1862, doi:10.1126/science.1211001.

Andrews, G. B., T. H. Zurbuchen, B. H. Mauk, H. Malcom, L. A. Fisk, G. Gloeckler, G. C. Ho, J. S. Kelley, P. L. Koehn, T. W. LeFevere, S. S. Livi, R. A. Lundgren, and J. M. Raines (2007), The energetic particle and plasma spectrometer instrument on the messenger spacecraft, *Space Science Reviews*, *131*(1), 523–556, doi:10.1007/s11214-007-9272-5.

Burlaga, L. F. (1988), Magnetic clouds and force-free fields with constant alpha, *Journal of Geophysical Research: Space Physics*, *93*(A7), 7217–7224, doi:10.1029/JA093iA07p07217.

Chen, Y., G. Tóth, P. Cassak, X. Jia, T. I. Gombosi, J. A. Slavin, S. Markidis, I. B. Peng, V. K. Jordanova, and M. G. Henderson (2017), Global three-dimensional simulation of earth's dayside reconnection using a two-way coupled magnetohydrodynamics with embedded particle-in-cell model: Initial results, *Journal of Geophysical Research: Space Physics*, *122*(10), 10,318–10,335, doi:10.1002/2017JA024186.

Dewey, R. M., J. A. Slavin, J. M. Raines, D. N. Baker, and D. J. Lawrence (2017), Energetic electron acceleration and injection during dipolarization events in mercury's magnetotail, *Journal of Geophysical Research: Space Physics*, *122*(12), 12,170–12,188, doi:10.1002/2017JA024617.

Dewey, R. M., J. M. Raines, W. Sun, J. A. Slavin, and G. Poh (2018), Messenger observations of fast plasma flows in mercury's magnetotail, *Geophysical Research Letters*, *45*(19), 10,110–10,118, doi:10.1029/2018GL079056.

DiBraccio, G. A., J. A. Slavin, S. M. Imber, D. J. Gershman, J. M. Raines, C. M. Jackman, S. A. Boardsen, B. J. Anderson, H. Korth, T. H. Zurbuchen, R. L. McNutt, and S. C. Solomon (2015), Messenger observations of flux ropes in mercury's magnetotail, *Planetary and Space Science*, *115*, 77 – 89, doi:https://doi.org/10.1016/j.pss.2014.12.016, solar wind interaction with the terrestrial planets.

Ding, Y., and Z. J. Rong (2018), A statistical survey on the magnetic field distribution in mercury's magnetotail current sheet based on messenger observations, *Chinese J. Geophys. (in Chinese)*, *61*(2), 411–422, doi:10.6038/cjg2018L0225.

Farrugia, C. J., B. Lavraud, R. B. Torbert, M. Argall, I. Kacem, W. Yu, L. Alm, J. Burch, C. T. Russell, J. Shuster, J. Dorelli, J. P. Eastwood, R. E. Ergun, S. Fuselier, D. Gershman, B. L. Giles, Y. V. Khotyaintsev, P. A. Lindqvist, H. Matsui, G. T. Marklund, T. D. Phan, K. Paulson, C. Pollock, and R. J. Strangeway (2016), Magnetospheric multiscale mission observations and non-force free modeling of a flux transfer event immersed in a super-alfvÃ©nic flow, *Geophysical Research Letters*, *43*(12), 6070–6077, doi:10.1002/2016GL068758.

Fear, R. C., L. Trenchi, J. C. Coxon, and S. E. Milan (2017), How much flux does a flux transfer event transfer?, *Journal of Geophysical Research: Space Physics*, *122*(12), 12,310–12,327, doi:10.1002/2017JA024730.

Gershman, D. J., J. A. Slavin, J. M. Raines, T. H. Zurbuchen, B. J. Anderson, H. Korth, D. N. Baker, and S. C. Solomon (2013), Magnetic flux pileup and plasma depletion in mercury's subsolar magnetosheath, *Journal of Geophysical Research: Space Physics*, *118*(11), 7181–7199, doi:10.1002/2013JA019244.

Gershman, D. J., J. A. Slavin, J. M. Raines, T. H. Zurbuchen, B. J. Anderson, H. Korth, D. N. Baker, and S. C. Solomon (2014), Ion kinetic properties in mercury's pre-midnight plasma sheet, *Geophysical Research Letters*, *41*(16), 5740–5747, doi:10.1002/2014GL060468.

Glassmeier, K.-H. (1997), The hermean magnetosphere and its ionosphere-magnetosphere coupling, *Planetary and Space Science*, *45*(1), 119 – 125, doi:https://doi.org/10.1016/S0032-0633(96)00095-5.

Harris, E. G. (1962), On a plasma sheath separating regions of oppositely directed magnetic field, *Il Nuovo Cimento (1955-1965)*, *23*(1), 115–121, doi:10.1007/BF02733547.

Hesse, M., and J. Birn (1991), Plasmoid evolution in an extended magnetotail, *Journal of Geophysical Research: Space Physics*, *96*(A4), 5683–5696, doi:10.1029/90JA02503.

Hidalgo, M. A., C. Cid, A. F. Viñas, and J. Sequeiros (2002), A non-force-free approach to the topology of magnetic clouds in the solar wind, *Journal of Geophysical Research: Space Physics*, *107*(A1), SSH1–1–SSH 1–7, doi:10.1029/2001JA900100.

Hones, E. W. (1977), Substorm processes in the magnetotail: Comments on 'on hot tenuous plasmas, fireballs, and boundary layers in the earth's magnetotail' by l. a. frank, k. l. ackerson, and r. p. lepping, *Journal of Geophysical Research*, *82*(35), 5633–5640, doi:10.1029/JA082i035p05633.

Hughes, W. J., and D. G. Sibeck (1987), On the 3-dimensional structure of plasmoids, *Geophysical Research Letters*, *14*(6), 636–639, doi:10.1029/GL014i006p00636.

Imber, S. M., and J. A. Slavin (2017), Messenger observations of magnetotail loading and unloading: Implications for substorms at mercury, *Journal of Geophysical Research: Space Physics*, *122*(11), 11,402–11,412, doi:10.1002/2017JA024332.

Imber, S. M., J. A. Slavin, H. U. Auster, and V. Angelopoulos (2011), A themis survey of flux ropes and traveling compression regions: Location of the near-earth reconnection site during solar minimum, *Journal of Geophysical Research: Space Physics*, *116*(A2), doi:10.1029/2010JA016026.

Jackman, C. M., C. S. Arridge, N. André, F. Bagenal, J. Birn, M. P. Freeman, X. Jia, A. Kidder, S. E. Milan, A. Radioti, J. A. Slavin, M. F. Vogt, M. Volwerk, and A. P. Walsh (2014), Large-scale structure and dynamics of the magnetotails of mercury, earth, jupiter and saturn, *Space Science Reviews*, *182*(1), 85–154, doi:10.1007/s11214-014-0060-8.

Kivelson, M. G., and K. K. Khurana (1995), Models of flux ropes embedded in a harris neutral sheet: Force-free solutions in low and high beta plasmas, *Journal of Geophysical Research: Space Physics*, *100*(A12), 23,637–23,645, doi:10.1029/95JA01548.

Lepping, R. P., J. A. Slavin, M. Hesse, J. A. Jones, and A. Szabo (1996), Analysis of magnetotail flux ropes with strong core fields: Isee 3 observations, *Journal of geomagnetism and geoelectricity*, *48*(5-6), 589–601, doi:10.5636/jgg.48.589.

Lundquist, S. (1950), Magnetohydrostatic fields, *Ark. Fys.*, *2*, 361–365.

Moldwin, M. B., and W. J. Hughes (1991), Plasmoids as magnetic flux ropes, *Journal of Geophysical Research: Space Physics*, *96*(A8), 14,051–14,064, doi:10.1029/91JA01167.

Nakamura, T. K. M., R. Nakamura, Y. Narita, W. Baumjohann, and W. Daughton (2016), Multi-scale structures of turbulent magnetic reconnection, *Physics of Plasmas*, *23*(5), 052,116, doi:10.1063/1.4951025.

Ness, N., K. Behannon, R. Lepping, and Y. Whang (1976), Observations of mercury's magnetic field, *Icarus*, *28*(4), 479 – 488, doi:https://doi.org/10.1016/0019-1035(76)90121-4.

Ogilvie, K. W., J. D. Scudder, V. M. Vasyliunas, R. E. Hartle, and G. L. Siscoe (1977), Observations at the planet mercury by the plasma electron experiment: Mariner 10, *Journal of Geophysical Research (1896-1977)*, *82*(13), 1807–1824, doi:10.1029/JA082i013p01807.

Paschmann, G., G. Haerendel, I. Papamastorakis, N. Sckopke, S. J. Bame, J. T. Gosling, and C. T. Russell (1982), Plasma and magnetic field characteristics of magnetic flux transfer events, *Journal of Geophysical Research: Space Physics*, *87*(A4), 2159–2168, doi:10.1029/JA087iA04p02159.

Poh, G., J. A. Slavin, X. Jia, J. M. Raines, S. M. Imber, W.-J. Sun, D. J. Gershman, G. A. DiBraccio, K. J. Genestreti, and A. W. Smith (2017a), Coupling between mercury and its nightside magnetosphere: Cross-tail current sheet asymmetry and substorm current wedge formation, *Journal of Geophysical Research: Space Physics*, *122*(8), 8419–8433, doi:10.1002/2017JA024266.

Poh, G., J. A. Slavin, X. Jia, J. M. Raines, S. M. Imber, W.-J. Sun, D. J. Gershman, G. A. DiBraccio, K. J. Genestreti, and A. W. Smith (2017b), Mercury's cross-tail current sheet: Structure, x-line location and stress balance, *Geophysical Research Letters*, *44*(2), 678–686, doi:10.1002/2016GL071612.

Poh, G., J. A. Slavin, X. Jia, W.-J. Sun, J. M. Raines, S. M. Imber, G. A. DiBraccio, and D. J. Gershman (2018), Transport of mass and energy in mercury's plasma sheet, *Geophysical Research Letters*, *45*(22), 12,163–12,170, doi:10.1029/2018GL080601.

Raines, J. M., J. A. Slavin, T. H. Zurbuchen, G. Gloeckler, B. J. Anderson, D. N. Baker, H. Korth, S. M. Krimigis, and R. L. McNutt (2011), Messenger observations of the plasma environment near mercury, *Planetary and Space Science*, *59*(15), 2004 – 2015, doi:https://doi.org/10.1016/j.pss.2011.02.004, mercury after the MESSENGER flybys.

Raines, J. M., D. J. Gershman, T. H. Zurbuchen, M. Sarantos, J. A. Slavin, J. A. Gilbert, H. Korth, B. J. Anderson, G. Gloeckler, S. M. Krimigis, D. N. Baker, R. L. McNutt, and S. C. Solomon (2013), Distribution and compositional variations of plasma ions in mercury's space environment: The first three mercury years of messenger observations, *Journal of Geophysical Research: Space Physics*, *118*(4), 1604–1619, doi:10.1029/2012JA018073.

Rong, Z. J., Y. Ding, J. A. Slavin, J. Zhong, G. Poh, W. J. Sun, Y. Wei, L. H. Chai, W. X. Wan, and C. Shen (2018), The magnetic field structure of mercury's magnetotail, *Journal of Geophysical Research: Space Physics*, *123*(1), 548–566, doi: 10.1002/2017JA024923.

Russell, C., D. Baker, and J. Slavin (1988), The magnetosphere of mercury, *Mercury*, pp. 514–561.

Russell, C. T., and R. J. Walker (1985), Flux transfer events at mercury, *Journal of Geophysical Research: Space Physics*, *90*(A11), 11,067–11,074, doi: 10.1029/JA090iA11p11067.

Schindler, K. (1974), A theory of the substorm mechanism, *Journal of Geophysical Research*, *79*(19), 2803–2810, doi:10.1029/JA079i019p02803.

Schindler, K., D. Pfirsch, and H. Wobig (1973), Stability of two-dimensional collision-free plasmas, *Plasma Physics*, *15*(12), 1165.

Slavin, J. A., and R. E. Holzer (1979), The effect of erosion on the solar wind stand-off distance at mercury, *Journal of Geophysical Research: Space Physics*, *84*(A5), 2076–2082, doi:10.1029/JA084iA05p02076.

Slavin, J. A., D. N. Baker, J. D. Craven, R. C. Elphic, D. H. Fairfield, L. A. Frank, A. B. Galvin, W. J. Hughes, R. H. Manka, D. G. Mitchell, I. G. Richardson, T. R. Sanderson, D. J. Sibeck, E. J. Smith, and R. D. Zwickl (1989), Cdaw 8 observations of plasmoid signatures in the geomagnetic tail: An assessment, *Journal of Geophysical Research: Space Physics*, *94*(A11), 15,153–15,175, doi:10.1029/JA094iA11p15153.

Slavin, J. A., R. P. Lepping, J. Gjerloev, D. H. Fairfield, M. Hesse, C. J. Owen, M. B. Moldwin, T. Nagai, A. Ieda, and T. Mukai (2003), Geotail observations of magnetic flux ropes in the plasma sheet, *Journal of Geophysical Research: Space Physics*, *108*(A1), SMP 10–1–SMP 10–18, doi:10.1029/2002JA009557.

Slavin, J. A., E. I. Tanskanen, M. Hesse, C. J. Owen, M. W. Dunlop, S. Imber, E. A. Lucek, A. Balogh, and K.-H. Glassmeier (2005), Cluster observations of traveling compression regions in the near-tail, *Journal of Geophysical Research: Space Physics*, *110*(A6), doi:10.1029/2004JA010878.

Slavin, J. A., S. M. Krimigis, M. H. Acuña, B. J. Anderson, D. N. Baker, P. L. Koehn, H. Korth, S. Livi, B. H. Mauk, S. C. Solomon, and T. H. Zurbuchen (2007), Messenger: Exploring mercury's magnetosphere, *Space Science Reviews*, *131*(1), 133–160, doi:10.1007/s11214-007-9154-x.

Slavin, J. A., M. H. Acuña, B. J. Anderson, D. N. Baker, M. Benna, S. A. Boardsen, G. Gloeckler, R. E. Gold, G. C. Ho, H. Korth, S. M. Krimigis, R. L. McNutt, J. M. Raines, M. Sarantos, D. Schriver, S. C. Solomon, P. Trávníček, and T. H. Zurbuchen (2009), Messenger observations of magnetic reconnection in mercury's magnetosphere, *Science*, *324*(5927), 606–610, doi:10.1126/science.1172011.

Slavin, J. A., B. J. Anderson, D. N. Baker, M. Benna, S. A. Boardsen, G. Gloeckler, R. E. Gold, G. C. Ho, H. Korth, S. M. Krimigis, R. L. McNutt, L. R. Nittler, J. M. Raines, M. Sarantos, D. Schriver, S. C. Solomon, R. D. Starr, P. M. Trávníček, and T. H. Zurbuchen (2010), Messenger observations of extreme loading and unloading of mercury's magnetic tail, *Science*, *329*(5992), 665–668, doi:10.1126/science.1188067.

Slavin, J. A., S. M. Imber, S. A. Boardsen, G. A. DiBraccio, T. Sundberg, M. Sarantos, T. Nieves-Chinchilla, A. Szabo, B. J. Anderson, H. Korth, T. H. Zurbuchen, J. M. Raines, C. L. Johnson, R. M. Winslow, R. M. Killen, R. L. McNutt, and S. C. Solomon

(2012a), Messenger observations of a flux-transfer-event shower at mercury, *Journal of Geophysical Research: Space Physics*, *117*(A12), doi:10.1029/2012JA017926.

Slavin, J. A., B. J. Anderson, D. N. Baker, M. Benna, S. A. Boardsen, R. E. Gold, G. C. Ho, S. M. Imber, H. Korth, S. M. Krimigis, R. L. McNutt Jr., J. M. Raines, M. Sarantos, D. Schriver, S. C. Solomon, P. Trávníček, and T. H. Zurbuchen (2012b), Messenger and mariner 10 flyby observations of magnetotail structure and dynamics at mercury, *Journal of Geophysical Research: Space Physics*, *117*(A1), doi:10.1029/2011JA016900.

Slavin, J. A., G. A. DiBraccio, D. J. Gershman, S. M. Imber, G. K. Poh, J. M. Raines, T. H. Zurbuchen, X. Jia, D. N. Baker, K.-H. Glassmeier, S. A. Livi, S. A. Boardsen, T. A. Cassidy, M. Sarantos, T. Sundberg, A. Masters, C. L. Johnson, R. M. Winslow, B. J. Anderson, H. Korth, R. L. McNutt, and S. C. Solomon (2014), Messenger observations of mercury's dayside magnetosphere under extreme solar wind conditions, *Journal of Geophysical Research: Space Physics*, *119*(10), 8087–8116, doi:10.1002/2014JA020319.

Smith, A. W., J. A. Slavin, C. M. Jackman, G.-K. Poh, and R. C. Fear (2017), Flux ropes in the hermean magnetotail: Distribution, properties, and formation, *Journal of Geophysical Research: Space Physics*, *122*(8), 8136–8153, doi:10.1002/2017JA024295.

Solomon, S. C., R. L. McNutt, R. E. Gold, M. H. Acuña, D. N. Baker, W. V. Boynton, C. R. Chapman, A. F. Cheng, G. Gloeckler, J. W. H. III, S. M. Krimigis, W. E. McClintock, S. L. Murchie, S. J. Peale, R. J. Phillips, M. S. Robinson, J. A. Slavin, D. E. Smith, R. G. Strom, J. I. Trombka, and M. T. Zuber (2001), The messenger mission to mercury: scientific objectives and implementation, *Planetary and Space Science*, *49*(14), 1445 – 1465, doi:https://doi.org/10.1016/S0032-0633(01)00085-X, returns to Mercury.

Sonnerup, B. U. O., and L. J. Cahill (1967), Magnetopause structure and attitude from explorer 12 observations, *Journal of Geophysical Research*, *72*(1), 171–183, doi: 10.1029/JZ072i001p00171.

Sonnerup, B. U. O., and M. Scheible (1998), Minimum and maximum variance analysis, *Analysis methods for multi-spacecraft data*, pp. 185–220.

Sun, W.-J., J. A. Slavin, S. Fu, J. M. Raines, Q.-G. Zong, S. M. Imber, Q. Shi, Z. Yao, G. Poh, D. J. Gershman, Z. Pu, T. Sundberg, B. J. Anderson, H. Korth, and D. N. Baker (2015a), Messenger observations of magnetospheric substorm activity in mercury's near magnetotail, *Geophysical Research Letters*, *42*(10), 3692–3699, doi:10.1002/2015GL064052.

Sun, W.-J., J. A. Slavin, S. Fu, J. M. Raines, T. Sundberg, Q.-G. Zong, X. Jia, Q. Shi, X. Shen, G. Poh, Z. Pu, and T. H. Zurbuchen (2015b), Messenger observations of alfvénic and compressional waves during mercury's substorms, *Geophysical Research Letters*, *42*(15), 6189–6198, doi:10.1002/2015GL065452.

Sun, W. J., S. Y. Fu, J. A. Slavin, J. M. Raines, Q. G. Zong, G. K. Poh, and T. H. Zurbuchen (2016), Spatial distribution of mercury's flux ropes and reconnection fronts: Messenger observations, *Journal of Geophysical Research: Space Physics*, *121*(8), 7590–7607, doi:10.1002/2016JA022787.

Sun, W. J., J. M. Raines, S. Y. Fu, J. A. Slavin, Y. Wei, G. K. Poh, Z. Y. Pu, Z. H. Yao, Q. G. Zong, and W. X. Wan (2017), Messenger observations of the energization and heating of protons in the near-mercury magnetotail, *Geophysical Research Letters*, *44*(16), 8149–8158, doi:10.1002/2017GL074276.

Sun, W. J., J. A. Slavin, R. M. Dewey, J. M. Raines, S. Y. Fu, Y. Wei, T. Karlsson, G. K. Poh, X. Jia, D. J. Gershman, Q. G. Zong, W. X. Wan, Q. Q. Shi, Z. Y. Pu, and D. Zhao (2018), A comparative study of the proton properties of magnetospheric substorms at earth and mercury in the near magnetotail, *Geophysical Research Letters*, *0*(0), doi:10.1029/2018GL079181.

Taylor, J. B. (1986), Relaxation and magnetic reconnection in plasmas, *Rev. Mod. Phys.*, *58*, 741–763, doi:10.1103/RevModPhys.58.741.

Winslow, R. M., B. J. Anderson, C. L. Johnson, J. A. Slavin, H. Korth, M. E. Purucker, D. N. Baker, and S. C. Solomon (2013), Mercury's magnetopause and bow shock from messenger magnetometer observations, *Journal of Geophysical Research: Space Physics*, *118*(5), 2213–2227, doi:10.1002/jgra.50237.

Zhao, C., C. T. Russell, R. J. Strangeway, S. M. Petrinec, W. R. Paterson, M. Zhou, B. J. Anderson, W. Baumjohann, K. R. Bromund, M. Chutter, D. Fischer, G. Le, R. Nakamura, F. Plaschke, J. A. Slavin, R. B. Torbert, and H. Y. Wei (2016), Force balance at the magnetopause determined with mms: Application to flux transfer events, *Geophysical Research Letters*, *43*(23), 11,941–11,947, doi:10.1002/2016GL071568.

Zhong, J., W. X. Wan, J. A. Slavin, Y. Wei, R. L. Lin, L. H. Chai, J. M. Raines, Z. J. Rong, and X. H. Han (2015), Mercury's three-dimensional asymmetric magnetopause, *Journal of Geophysical Research: Space Physics*, *120*(9), 7658–7671, doi:10.1002/2015JA021425.

Zhong, J., Y. Wei, Z. Y. Pu, X. G. Wang, W. X. Wan, J. A. Slavin, X. Cao, J. M. Raines, H. Zhang, C. J. Xiao, A. M. Du, R. S. Wang, R. M. Dewey, L. H. Chai, Z. J. Rong, and Y. Li (2018), Messenger observations of rapid and impulsive magnetic reconnection in mercury's magnetotail, *The Astrophysical Journal Letters*, *860*(2), L20.

Zong, Q.-G., B. Wilken, G. D. Reeves, I. A. Daglis, T. Doke, T. Iyemori, S. Livi, K. Maezawa, T. Mukai, S. Kokubun, Z.-Y. Pu, S. Ullaland, J. Woch, R. Lepping, and T. Yamamoto (1997), Geotail observations of energetic ion species and magnetic field in plasmoid-like structures in the course of an isolated substorm event, *Journal of Geophysical Research: Space Physics*, *102*(A6), 11,409–11,428, doi:10.1029/97JA00076.

Zong, Q.-G., T. Fritz, H. Spence, M. Dunlop, Z. Pu, A. Korth, P. Daly, A. Balogh, and H. Reme (2003), Bursty energetic electrons confined in flux ropes in the cusp region, *Planetary and Space Science*, *51*(12), 821 – 830, doi:https://doi.org/10.1016/S0032-0633(03)00116-8, key Problems in Space Physics: Thin Magnetospheric Boundaries.

Zong, Q.-G., T. A. Fritz, Z. Y. Pu, S. Y. Fu, D. N. Baker, H. Zhang, A. T. Lui, I. Vogiatzis, K.-H. Glassmeier, A. Korth, P. W. Daly, A. Balogh, and H. Reme (2004), Cluster observations of earthward flowing plasmoid in the tail, *Geophysical Research Letters*, *31*(18), doi:10.1029/2004GL020692.

Table 1: The start and end times of the MESSENGER hot seasons

#	year	start doy[a]	end doy
1	2011	309	335
2	2012	33	58
3	2012	122	144
4	2012	210	232
5	2012	297	318
6	2013	64	79
7	2013	146	163
8	2013	231	254
9	2013	318	342
10	2014	43	65
11	2014	132	151
12	2014	218	238
13	2014	305	328
14	2015	27	52

[a] doy, day of the year

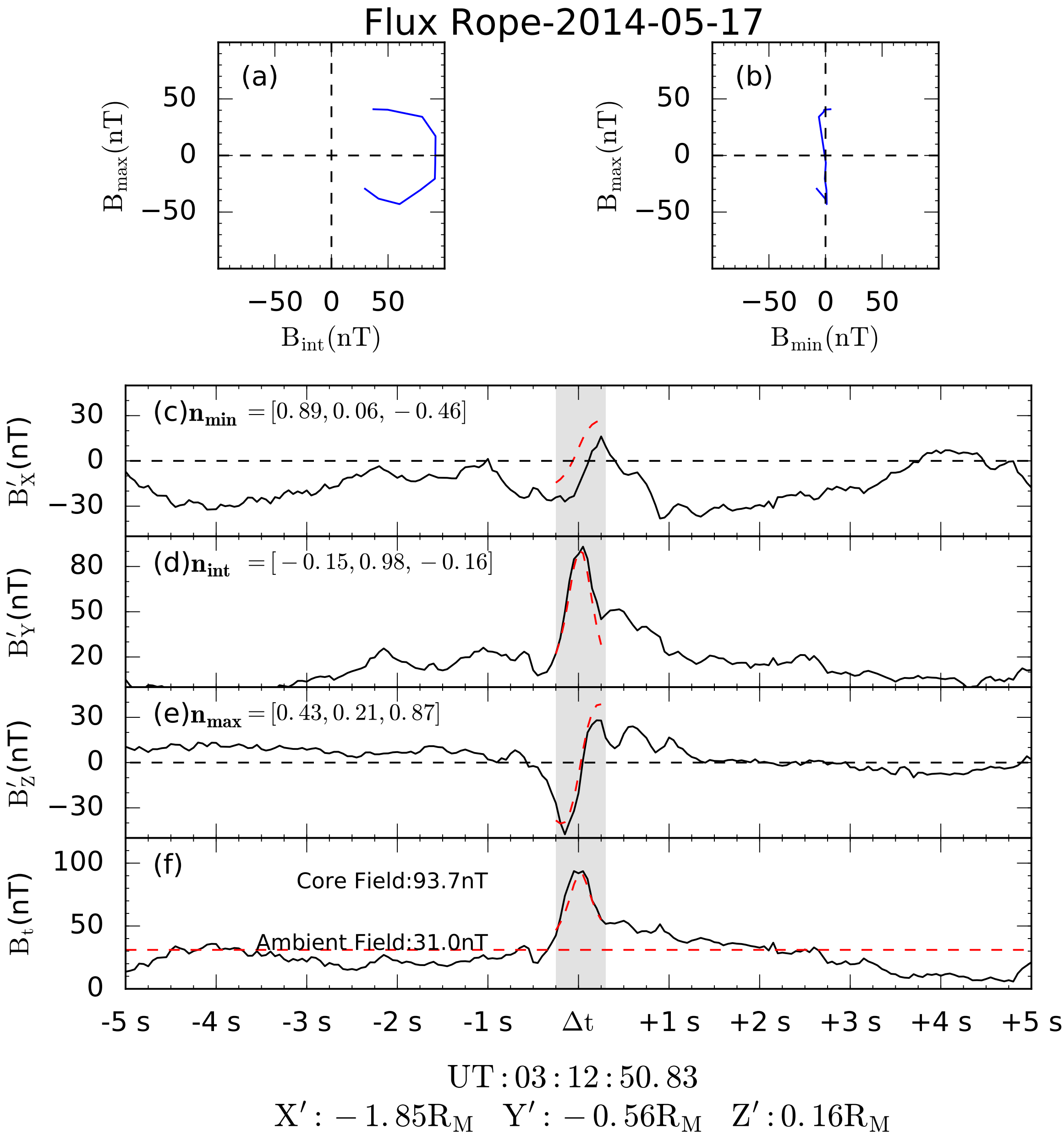

Figure 1: A flux rope case in Mercury's magnetotail at ∼ 03:12:50.83 UT, 17 May 2014. MVA magnetic field hodograms of the flux rope are shown in the planes of B_{max} - B_{int} (a) and B_{max} - B_{min} (b), respectively. (c) magnetic field x component, B_{x}, (d) B_{y}, (e) B_{z}, (f) B_{t}. Dashed red curves in the shaded region from (c) to (f) are the magnetic field from the fitting of KK95 model.

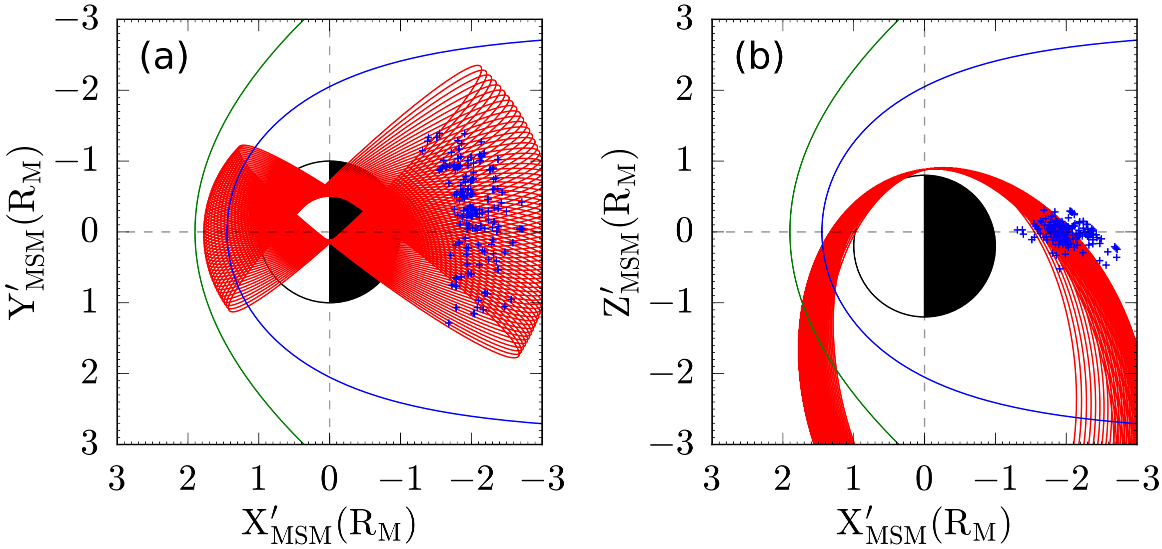

Figure 2: Spatial distributions of the 168 flux ropes in $X'_{MSM} - Y'_{MSM}$ (a) and $X'_{MSM} - Z'_{MSM}$ (b) planes, respectively. Blue crosses represent the flux ropes. MESSENGER orbits in the hot season from 2011-309 to 2011-335 are shown as red lines. The blue and green lines indicate the average locations of magnetopause and bow shock of Mercury's magnetosphere from [*Winslow et al.*, 2013].

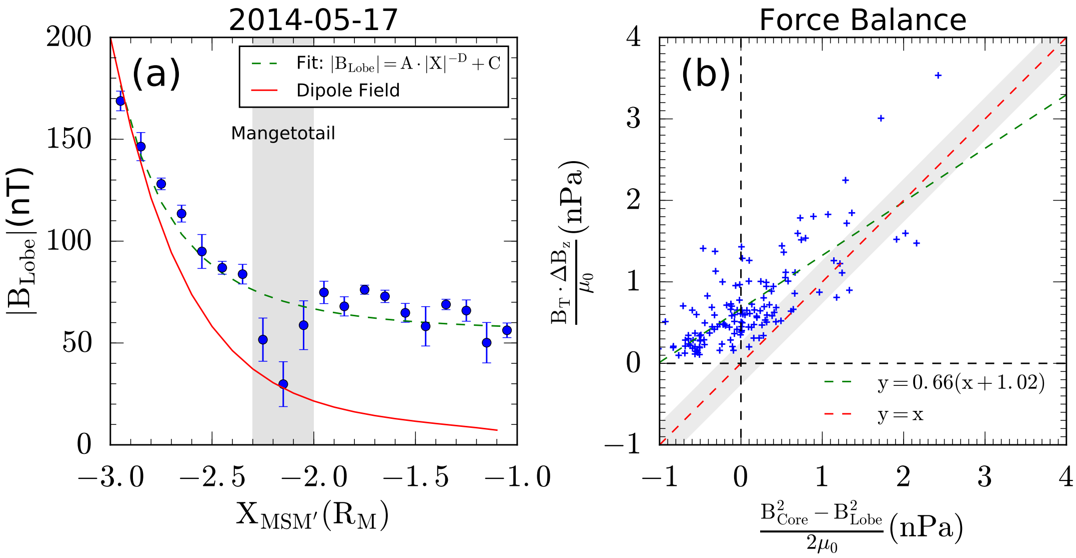

Figure 3: (a) Power Law fitting of the magnetic field intensity (B_t) along the tail distance (X'_{MSM}) for the first magnetotail passes on 17 May 2014. The red line indicates the magnitude of the dipole magnetic field of Mercury. The blue dots with error bars represent the intensities of the measured magnetic field, which are averaged over each 0.1 R_M bin (error bars here are the standard deviation). The dashed green line shows the power law fitting of the blue dots with the parameters A = 144.8 nT, D = 3.7 and C = 55.5 nT. (b) The distribution of magnetic pressure differences and magnetic tension force for the 143 flux ropes. Each cross indicates an event. The dashed red line has a slope of one. The dashed green line is the linear fit of the data points. The shaded region corresponding to the quasi-force-free criterion.

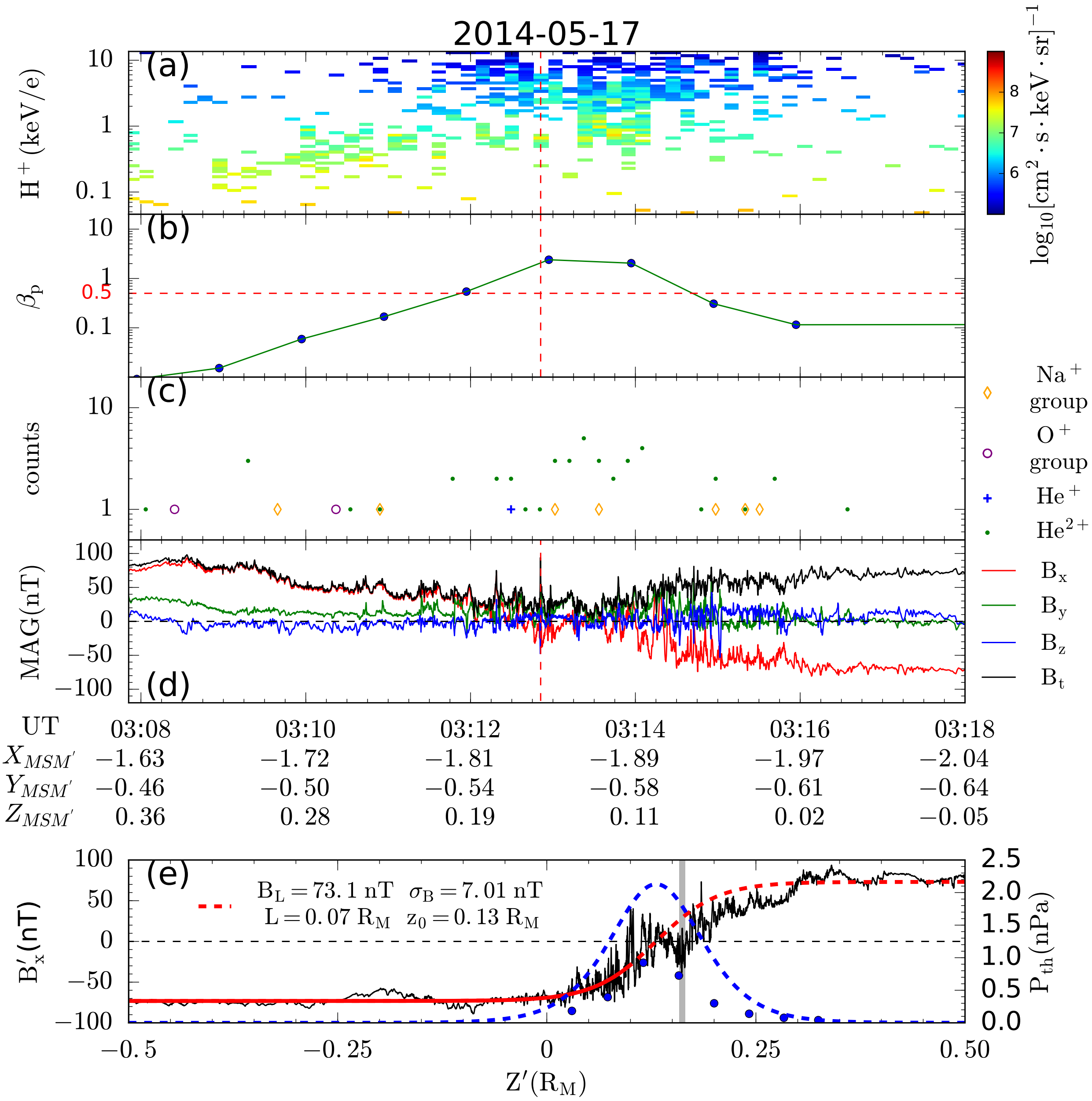

Figure 4: Plasma and magnetic field measurements from MESSENGER between 03:08 to 03:18 UT on 17 May 2014. (a) energy spectrum for proton differential particle flux, (b) plasma β from one minute average proton moments, (c) heavy ion counts of four composition types, He^{+} (cross), He^{++} (dots), O^{+} group, m/q = 14–20, (circle), and Na^{+} group, $m/q = 20 - 30$, (diamond), (d) magnetic field components, B_x (red), B_y (green), B_z (blue), B_t (black), (e) B'_x measurements in local coordinate (black) and the fitting from Harris current sheet model (red), thermal pressure from Harris current sheet fitting (dashed blue line), thermal pressure from one minute proton moments (blue dots).

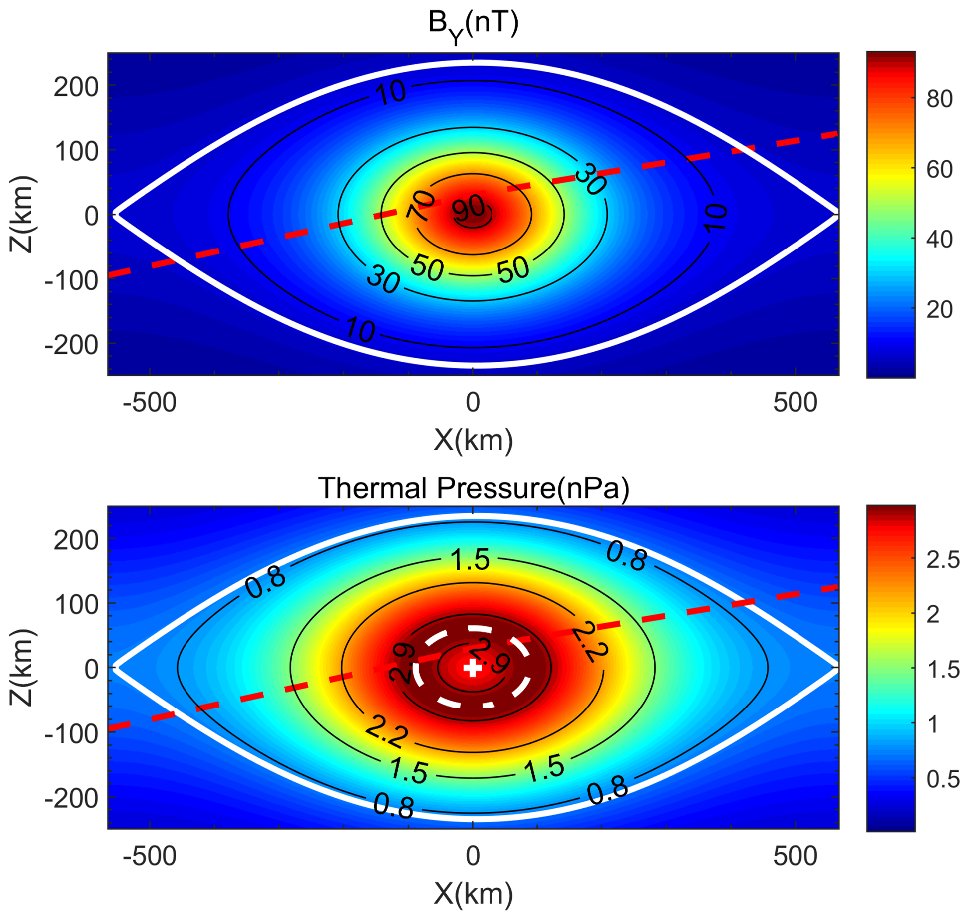

Figure 5: The core field, B_y, (a) and thermal pressure, p, (b) distributions from the KK95 model for the flux rope in Figure 1. The dashed red line represents the trajectory of the spacecraft. Solid white line marks the boundary of the flux rope. Dashed white line and cross indicates the contour of peak ($p = 2.98$nPa) and the central dip ($p = 2.75$nPa) of thermal pressure in the flux rope. Black lines with values are the contour of B_y and p.

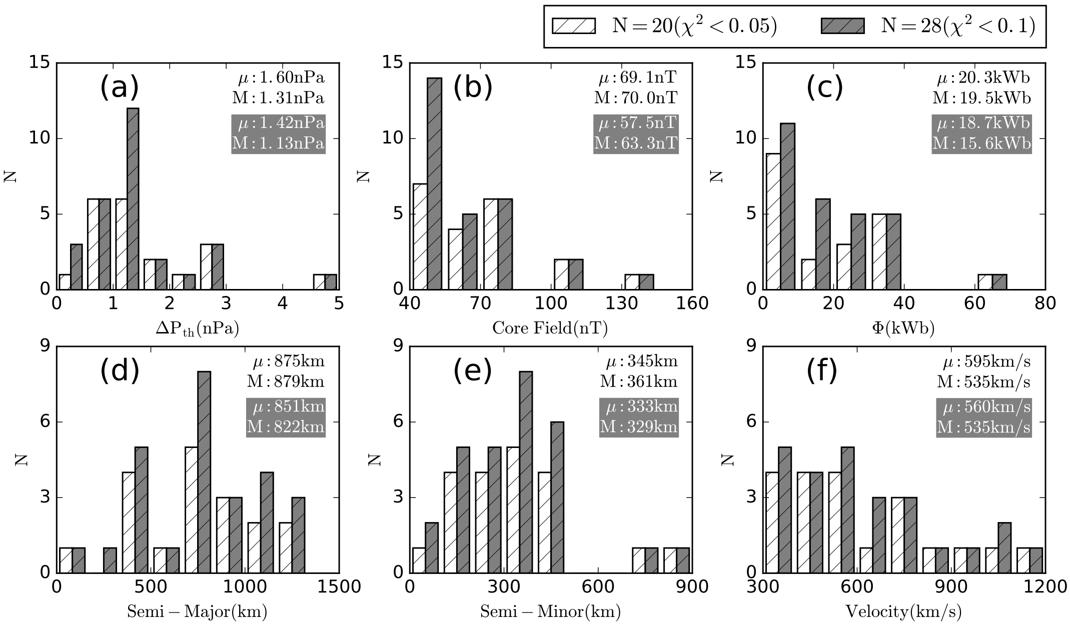

Figure 6: Statistical properties of the flux ropes resulted from the KK95 model. (a) The largest thermal pressure (p) difference along the major axes, (b) the core field in the center of flux rope, (c) magnetic flux content, (d) semi-major axes (scale in X'_{MSM}), (e) semi-minor axes (scale in Z'_{MSM}), (f) The traveling speeds. The grey and white bars represent the distributions of event with $\chi^2 < 0.1$ and $\chi^2 < 0.05$, respectively. In each figure, μ represent the mean values. M represent the median values.

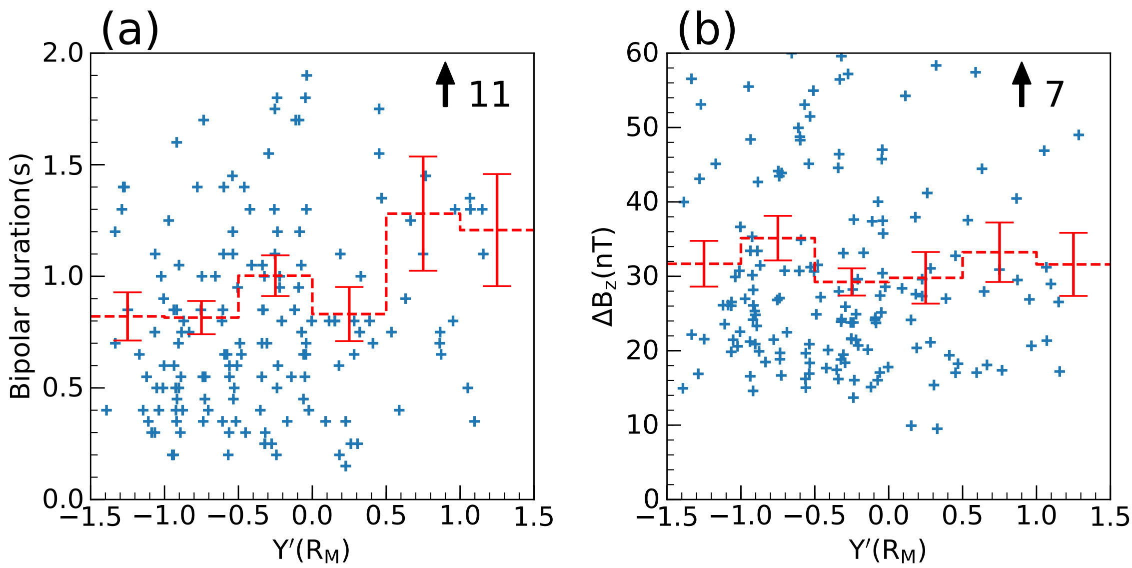

Figure 7: The distributions of the duration and amplitudes of flux ropes along Y'_{MSM}. (a) the duration were obtained from peak to peak of B_z. (b) the amplitude of B_z from peak to peak. Errorbars represent the standard error of the mean in each bin. Number of off-axis events is marked on the top right corner.Another version of this Figure with a wider range in Y-axis is attached in supplementary material as Figure S2.

Figure1.

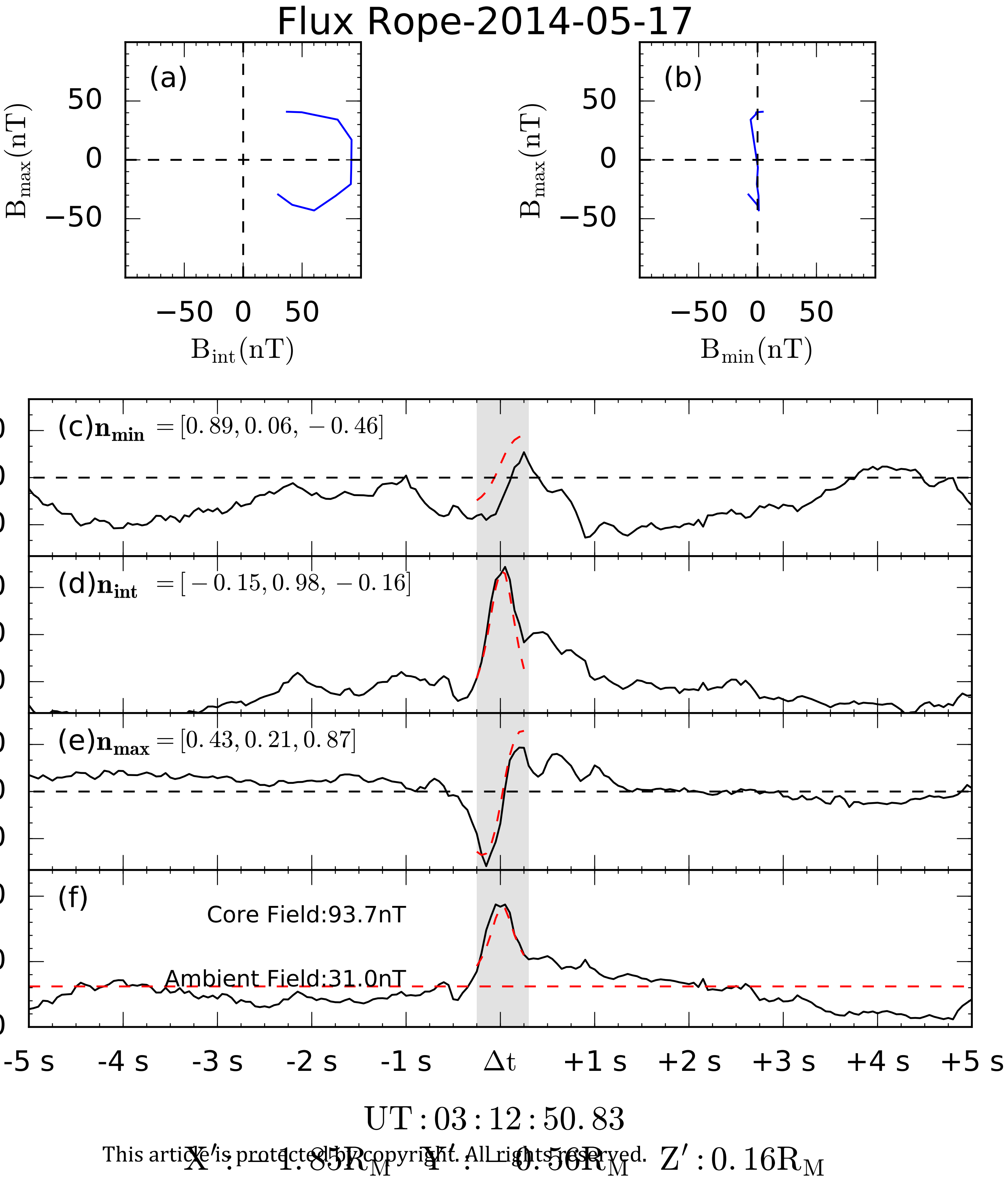
Flux Rope-2014-05-17
(a)
(b)
$B_{max}(nT)$
$B_{int}(nT)$
$B_{min}(nT)$
50
0
−50
(c)$\mathbf{n_{min}} = [0.89, 0.06, -0.46]$
(d)$\mathbf{n_{int}} = [-0.15, 0.98, -0.16]$
(e)$\mathbf{n_{max}} = [0.43, 0.21, 0.87]$
(f)
$B'_X(nT)$
$B'_Y(nT)$
$B'_Z(nT)$
$B_t(nT)$
Core Field:93.7nT
Ambient Field:31.0nT
-5 s
-4 s
-3 s
-2 s
-1 s
Δt
+1 s
+2 s
+3 s
+4 s
+5 s
$UT: 03:12:50.83$
$X': -1.85R_M$ $Y': -0.56R_M$ $Z': 0.16R_M$

Figure2.

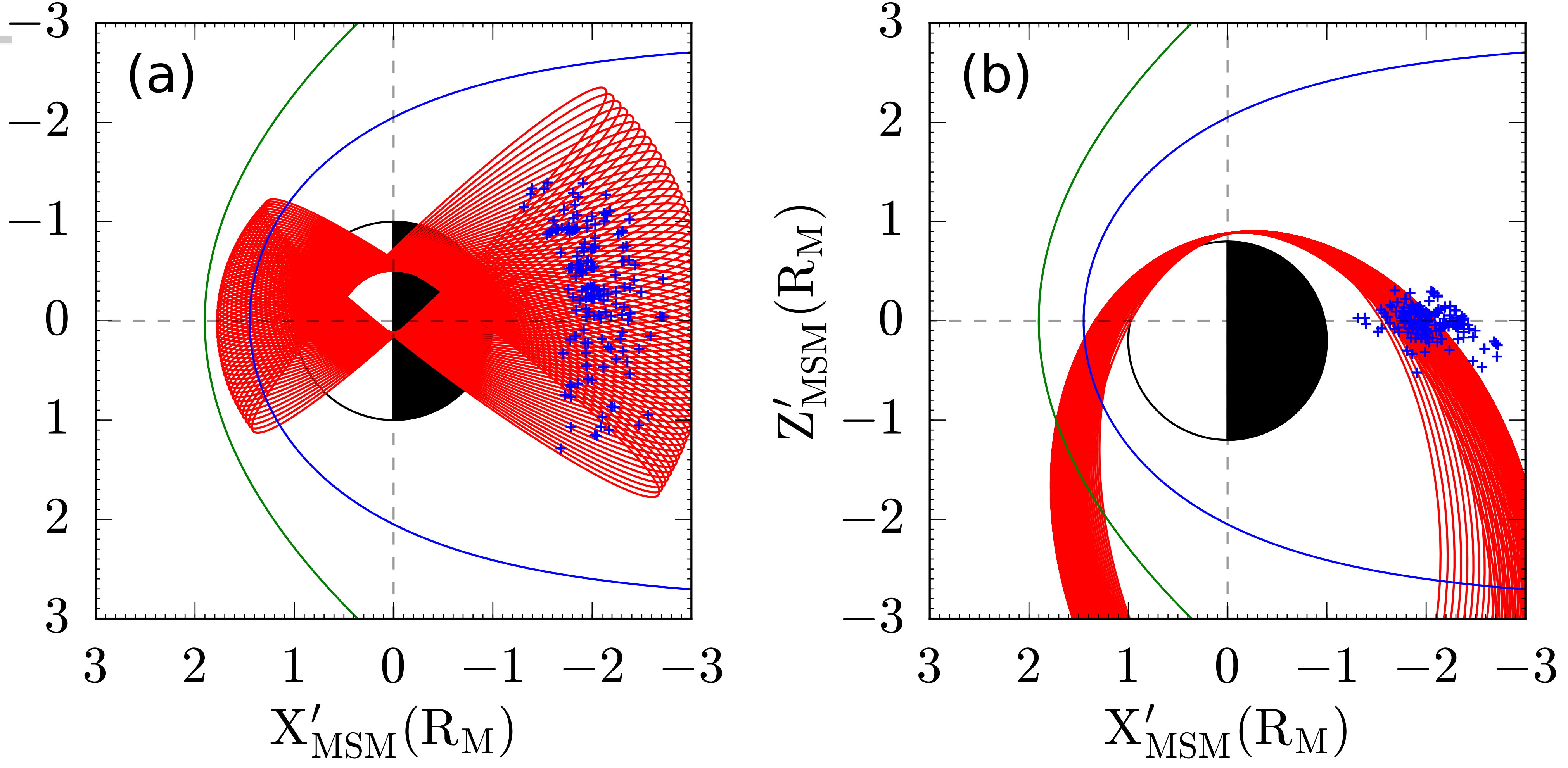
(a)
(b)
Y′MSM(RM)
Z′MSM(RM)
X′MSM(RM)
X′MSM(RM)
−3
−2
−1
0
1
2
3
3
2
1
0
−1
−2
−3

Figure3.

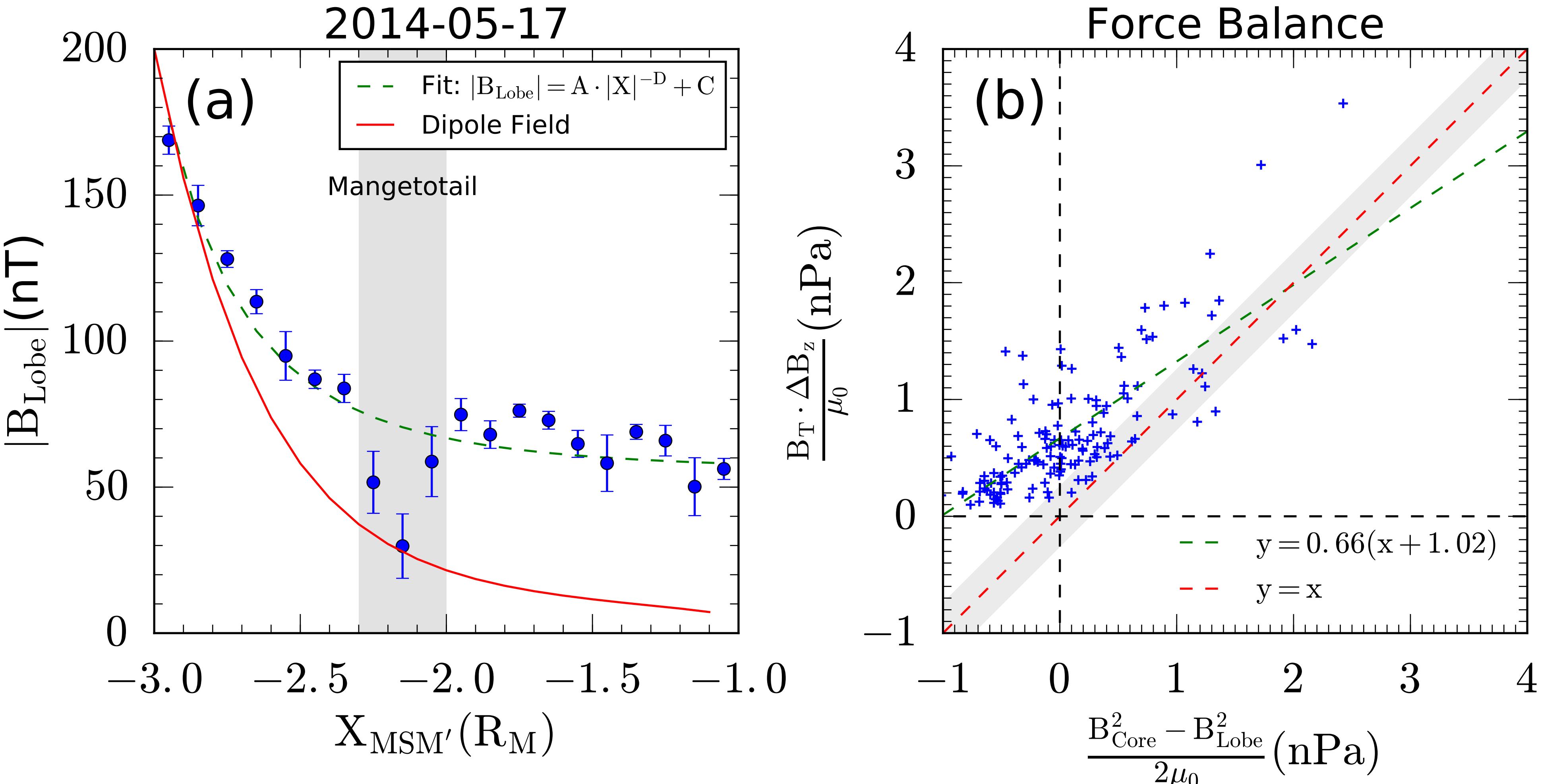

2014-05-17
(a)
Fit: $|B_{Lobe}| = A \cdot |X|^{-D} + C$
Dipole Field
Mangetotail
$|B_{Lobe}|$(nT)
$X_{MSM'}(R_M)$
Force Balance
(b)
$\frac{B_T \cdot \Delta B_z}{\mu_0}$(nPa)
$\frac{B^2_{Core} - B^2_{Lobe}}{2\mu_0}$(nPa)
$y = 0.66(x + 1.02)$
$y = x$

Figure4.

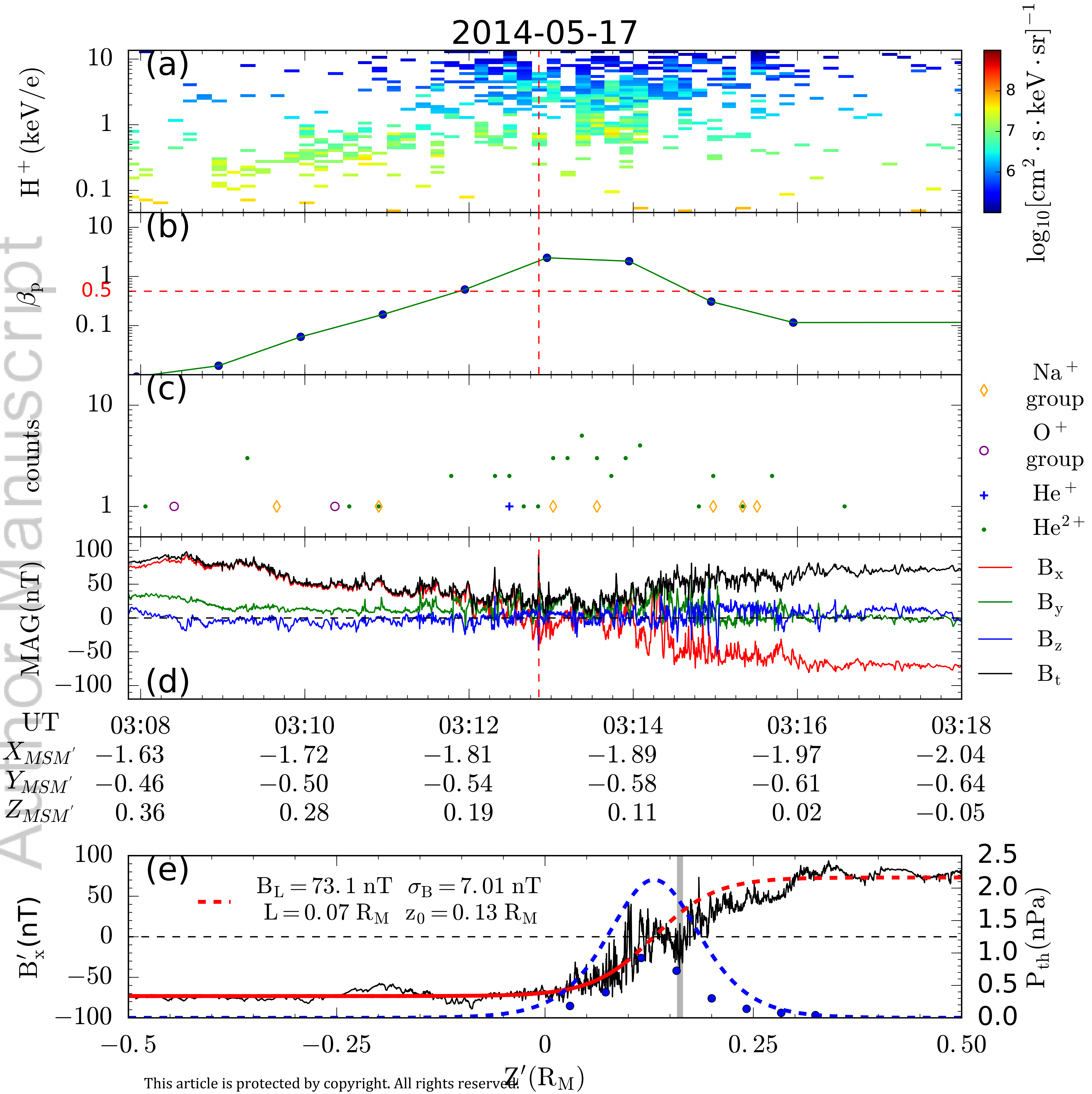
2014-05-17
(a)
(b)
(c)
(d)
(e)
H^+ (keV/e)
β_p
0.5
counts
MAG(nT)
$\log_{10}[cm^2 \cdot s \cdot keV \cdot sr]^{-1}$
Na^+ group
O^+ group
He^+
He^{2+}
B_x
B_y
B_z
B_t
UT 03:08 03:10 03:12 03:14 03:16 03:18
$X_{MSM'}$ −1.63 −1.72 −1.81 −1.89 −1.97 −2.04
$Y_{MSM'}$ −0.46 −0.50 −0.54 −0.58 −0.61 −0.64
$Z_{MSM'}$ 0.36 0.28 0.19 0.11 0.02 −0.05
$B_L = 73.1$ nT $\sigma_B = 7.01$ nT
$L = 0.07\ R_M$ $z_0 = 0.13\ R_M$
B'_x(nT)
P_{th}(nPa)
$Z'(R_M)$

Figure5.

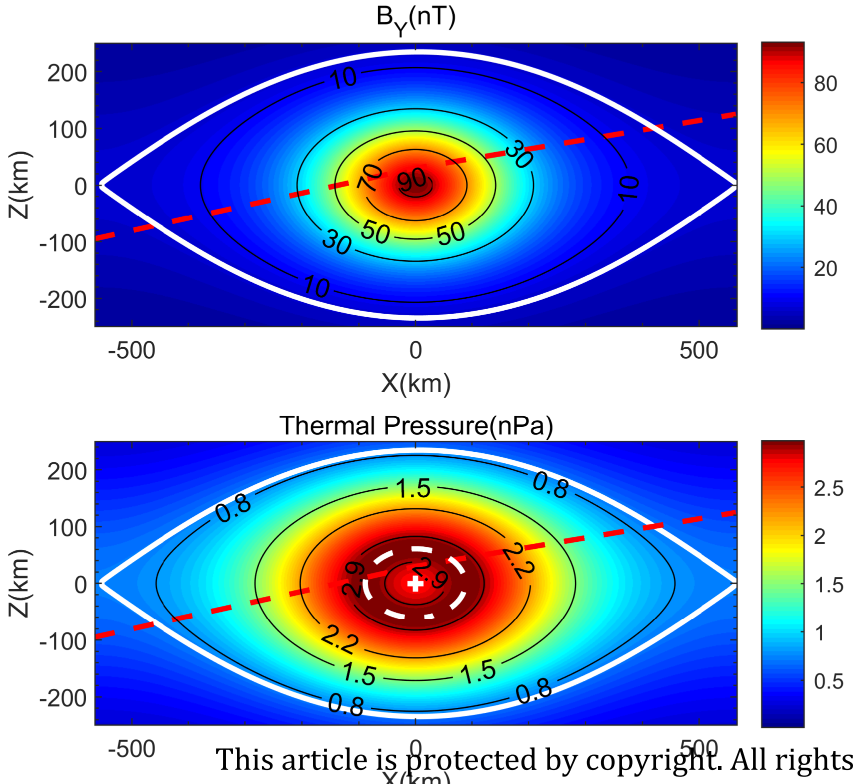

B_Y(nT)
Z(km)
X(km)
200
100
0
-100
-200
-500
0
500
10
30
50
70
90
80
60
40
20
Thermal Pressure(nPa)
0.8
1.5
2.2
2.9
2.5
2
1
0.5

Figure6.

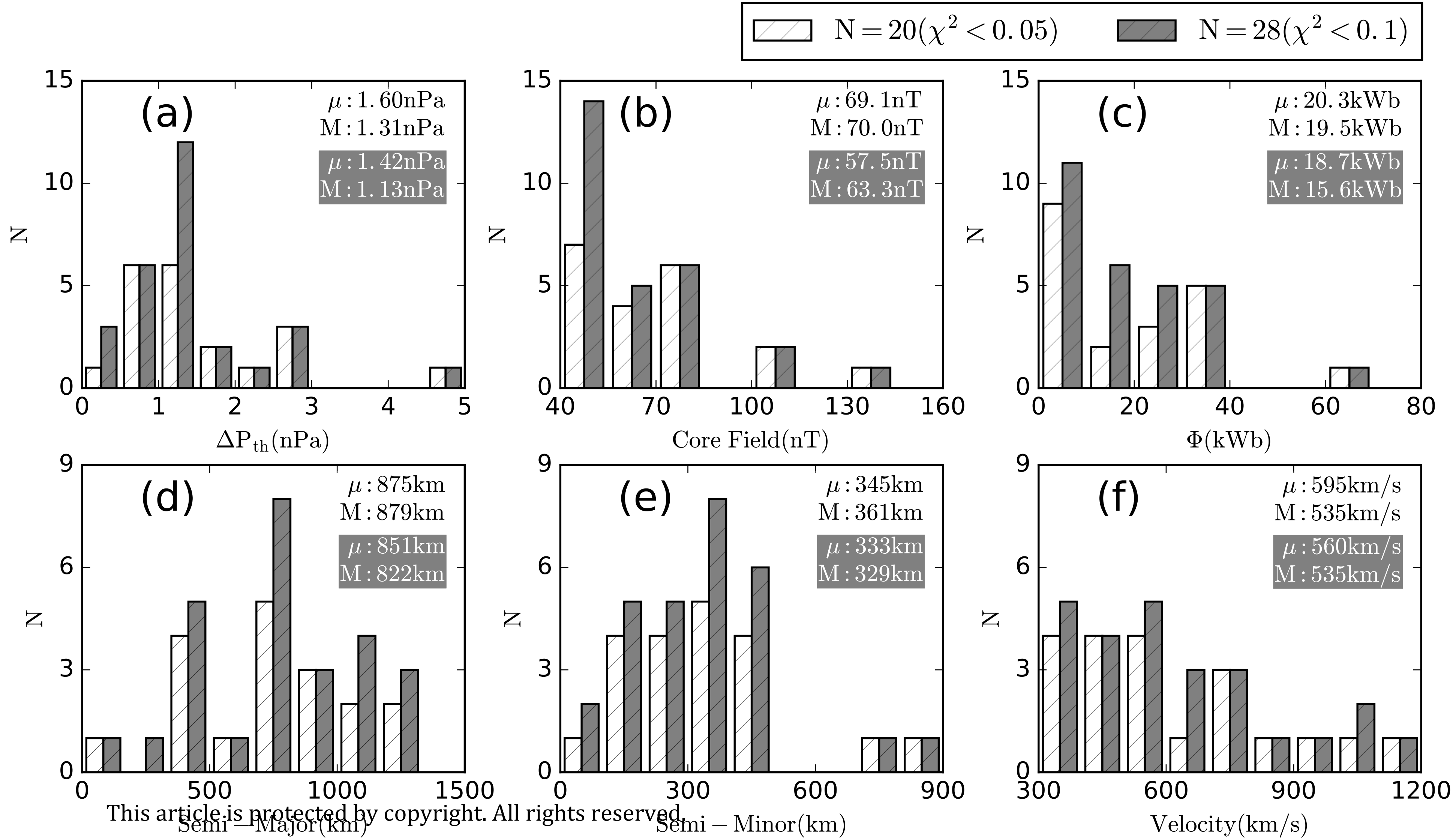
N = 20(χ² < 0.05)
N = 28(χ² < 0.1)
(a)
μ : 1.60nPa
M : 1.31nPa
μ : 1.42nPa
M : 1.13nPa
ΔP_th(nPa)
(b)
μ : 69.1nT
M : 70.0nT
μ : 57.5nT
M : 63.3nT
Core Field(nT)
(c)
μ : 20.3kWb
M : 19.5kWb
μ : 18.7kWb
M : 15.6kWb
Φ(kWb)
(d)
μ : 875km
M : 879km
μ : 851km
M : 822km
Semi − Major(km)
(e)
μ : 345km
M : 361km
μ : 333km
M : 329km
Semi − Minor(km)
(f)
μ : 595km/s
M : 535km/s
μ : 560km/s
M : 535km/s
Velocity(km/s)
N

Figure7.

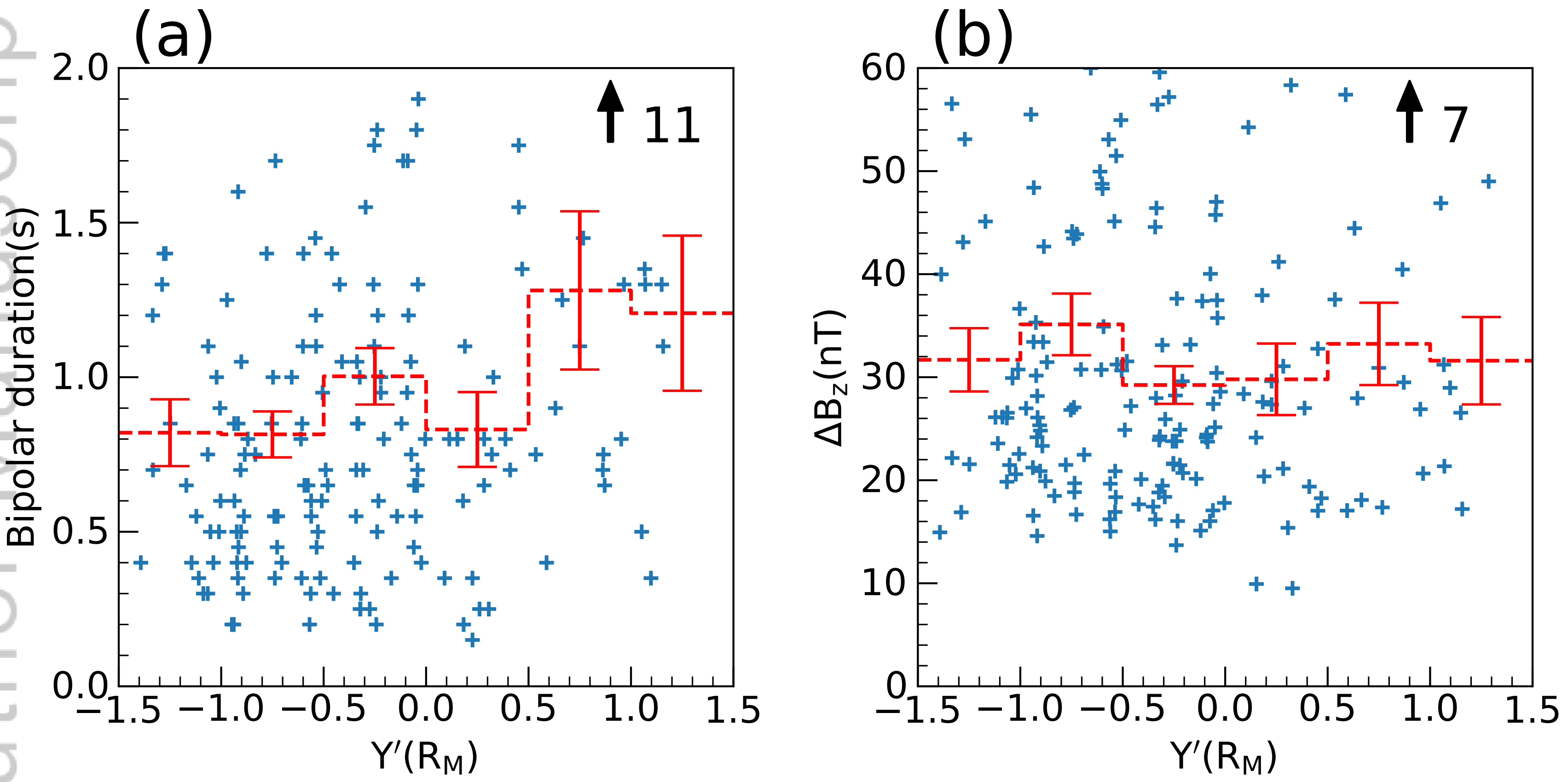
(a)
(b)
Bipolar duration(s)
ΔBz(nT)
Y′(RM)
Y′(RM)
11
7
2.0
1.5
1.0
0.5
0.0
60
50
40
30
20
10
0
−1.5 −1.0 −0.5 0.0 0.5 1.0 1.5

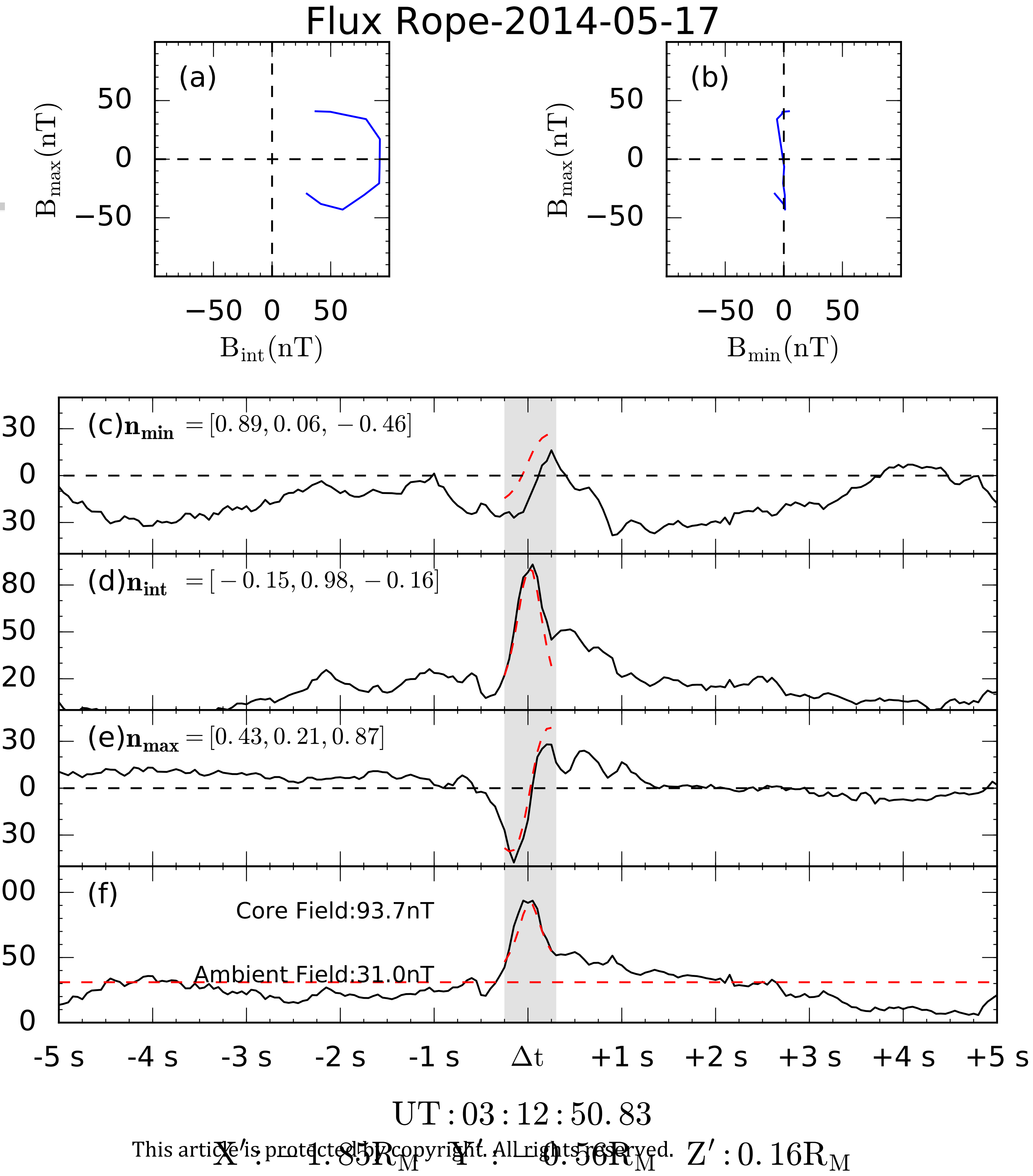
Flux Rope-2014-05-17
(a)
(b)
$B_{max}(nT)$
$B_{int}(nT)$
$B_{min}(nT)$
(c)$\mathbf{n_{min}} = [0.89, 0.06, -0.46]$
(d)$\mathbf{n_{int}} = [-0.15, 0.98, -0.16]$
(e)$\mathbf{n_{max}} = [0.43, 0.21, 0.87]$
(f)
Core Field:93.7nT
Ambient Field:31.0nT
$B'_X(nT)$
$B'_Y(nT)$
$B'_Z(nT)$
$B_t(nT)$
-5 s
-4 s
-3 s
-2 s
-1 s
Δt
+1 s
+2 s
+3 s
+4 s
+5 s
$UT: 03:12:50.83$
$X': -1.85R_M$ $Y': -0.56R_M$ $Z': 0.16R_M$

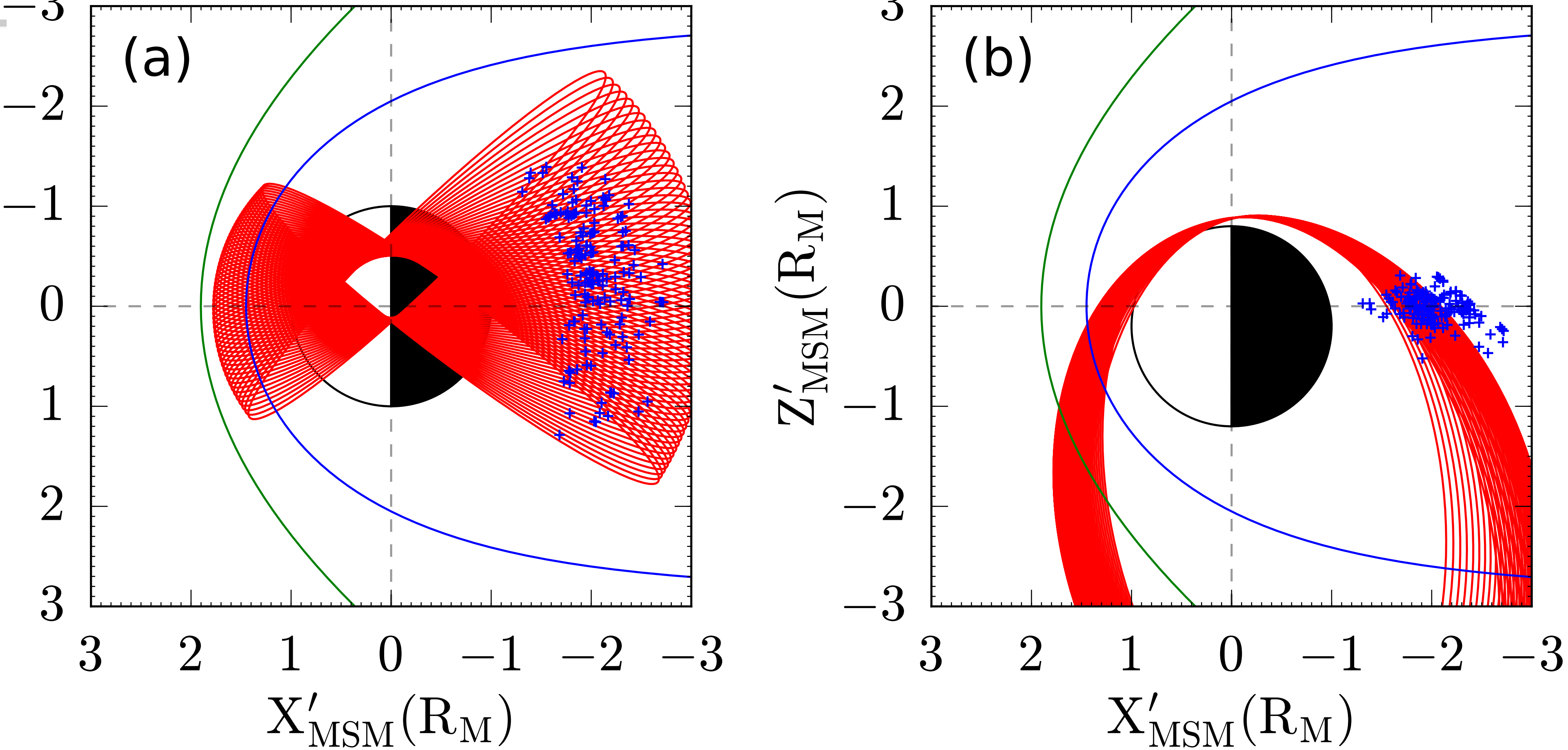

(a)
(b)
−3
−2
−1
0
1
2
3
3
2
1
0
−1
−2
−3
$Y'_{MSM}(R_M)$
$Z'_{MSM}(R_M)$
$X'_{MSM}(R_M)$
$X'_{MSM}(R_M)$

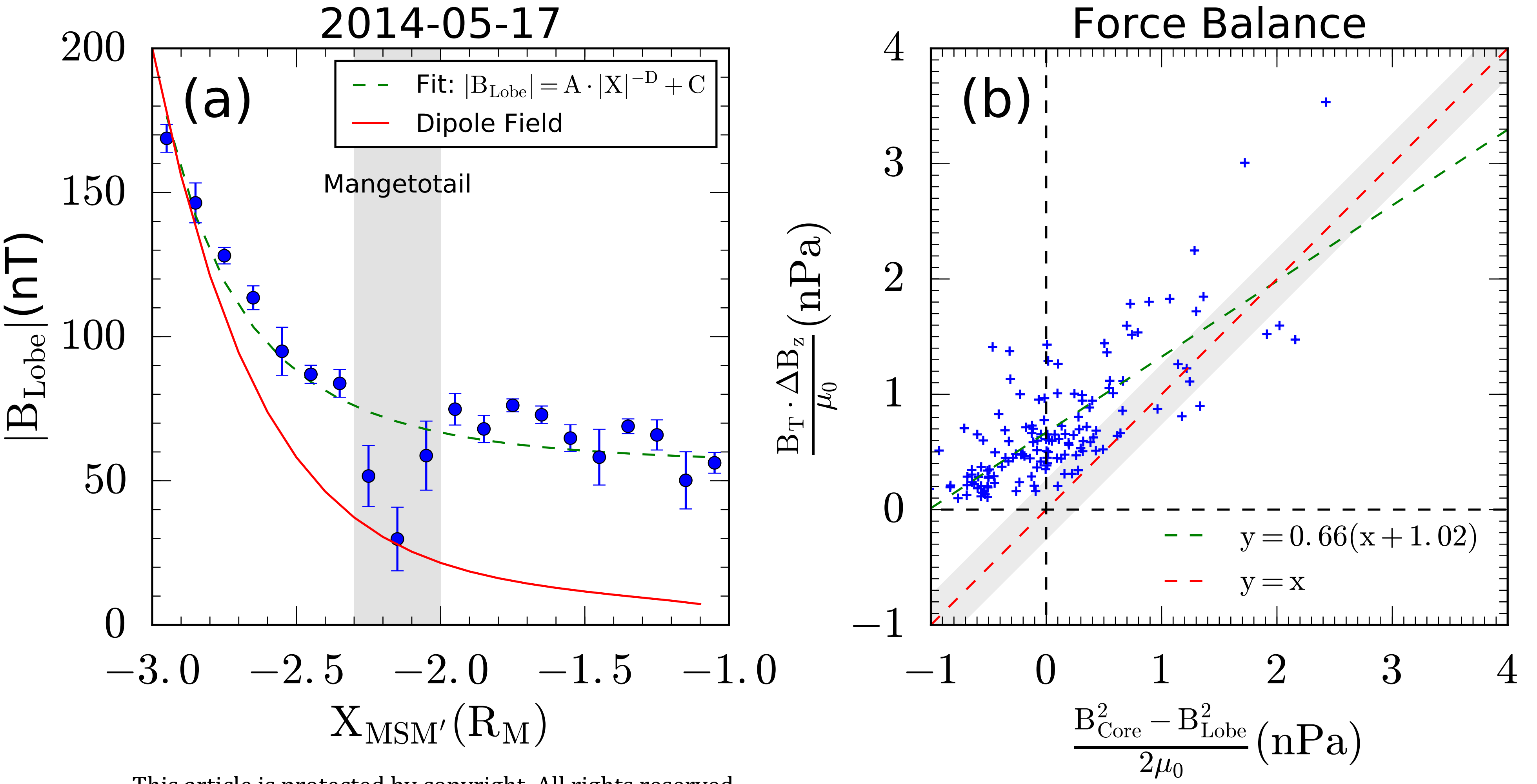

2014-05-17
(a)
Fit: |B_Lobe| = A · |X|^−D + C
Dipole Field
Mangetotail
|B_Lobe| (nT)
200
150
100
50
0
−3.0
−2.5
−2.0
−1.5
−1.0
X_MSM′ (R_M)
Force Balance
(b)
B_T · ΔB_z / μ_0 (nPa)
(B²_Core − B²_Lobe) / 2μ_0 (nPa)
y = 0.66(x + 1.02)
y = x
4
3
2
1
0
−1

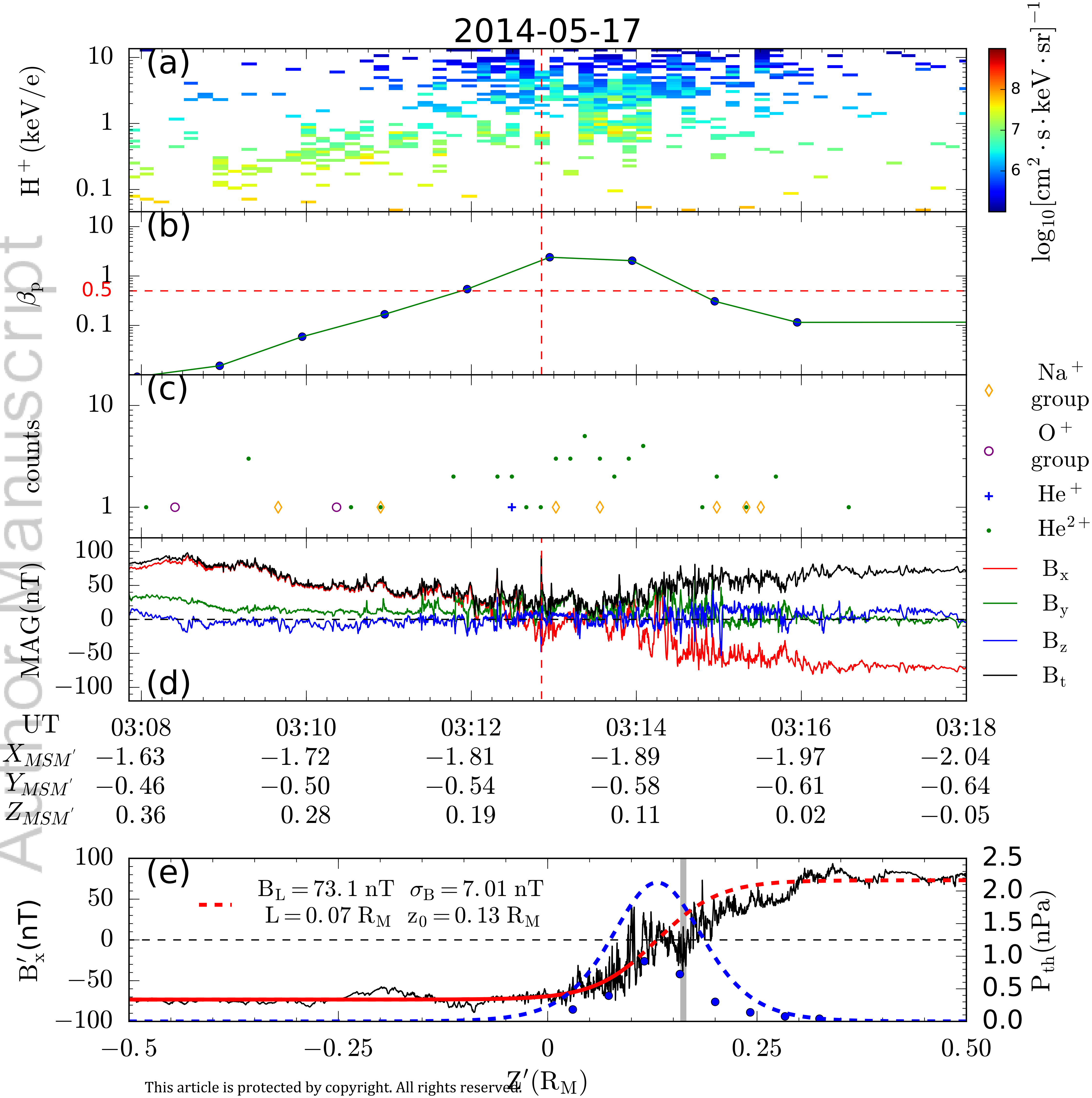
2014-05-17
(a)
H$^+$ (keV/e)
10
1
0.1
$\log_{10}[\mathrm{cm}^2 \cdot \mathrm{s} \cdot \mathrm{keV} \cdot \mathrm{sr}]^{-1}$
8
7
6
(b)
β_p
0.5
(c)
counts
Na^+ group
O^+ group
He^+
He^{2+}
(d)
MAG(nT)
100
50
0
−50
−100
B_x
B_y
B_z
B_t
UT 03:08 03:10 03:12 03:14 03:16 03:18
$X_{MSM'}$ −1.63 −1.72 −1.81 −1.89 −1.97 −2.04
$Y_{MSM'}$ −0.46 −0.50 −0.54 −0.58 −0.61 −0.64
$Z_{MSM'}$ 0.36 0.28 0.19 0.11 0.02 −0.05
(e)
$B_L = 73.1$ nT $\sigma_B = 7.01$ nT
$L = 0.07\ R_M$ $z_0 = 0.13\ R_M$
B'_x(nT)
P_{th}(nPa)
2.5
2.0
1.5
1.0
0.5
0.0
−0.5 −0.25 0 0.25 0.50
$Z'(R_M)$

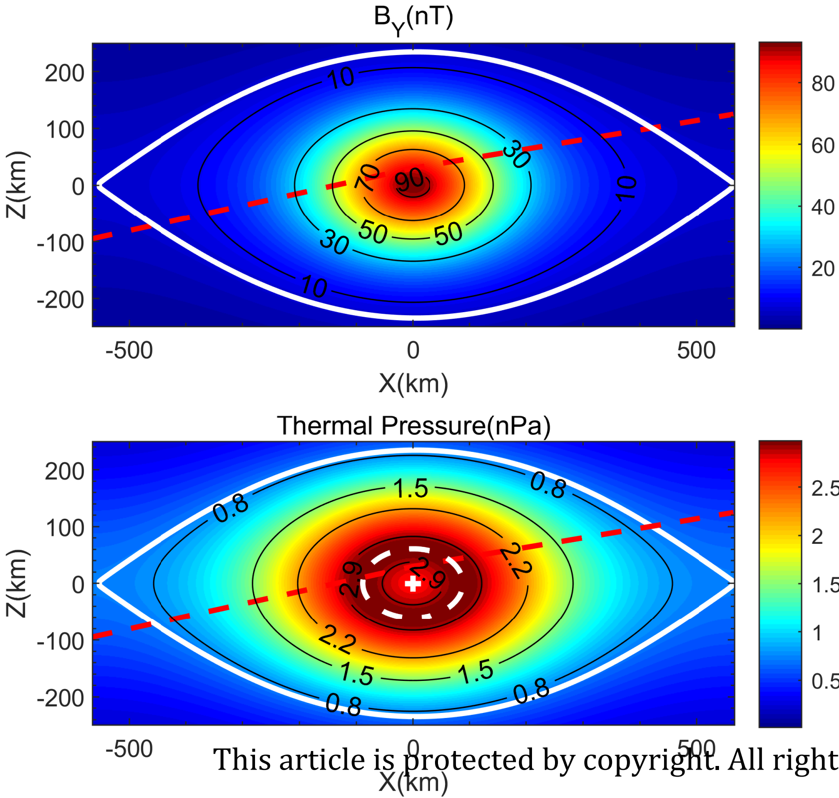

B_Y(nT)
Z(km)
X(km)
200
100
0
-100
-200
-500
0
500
10
30
50
70
90
80
60
40
20
Thermal Pressure(nPa)
0.8
1.5
2.2
2.9
2.5
2
1.5
1
0.5

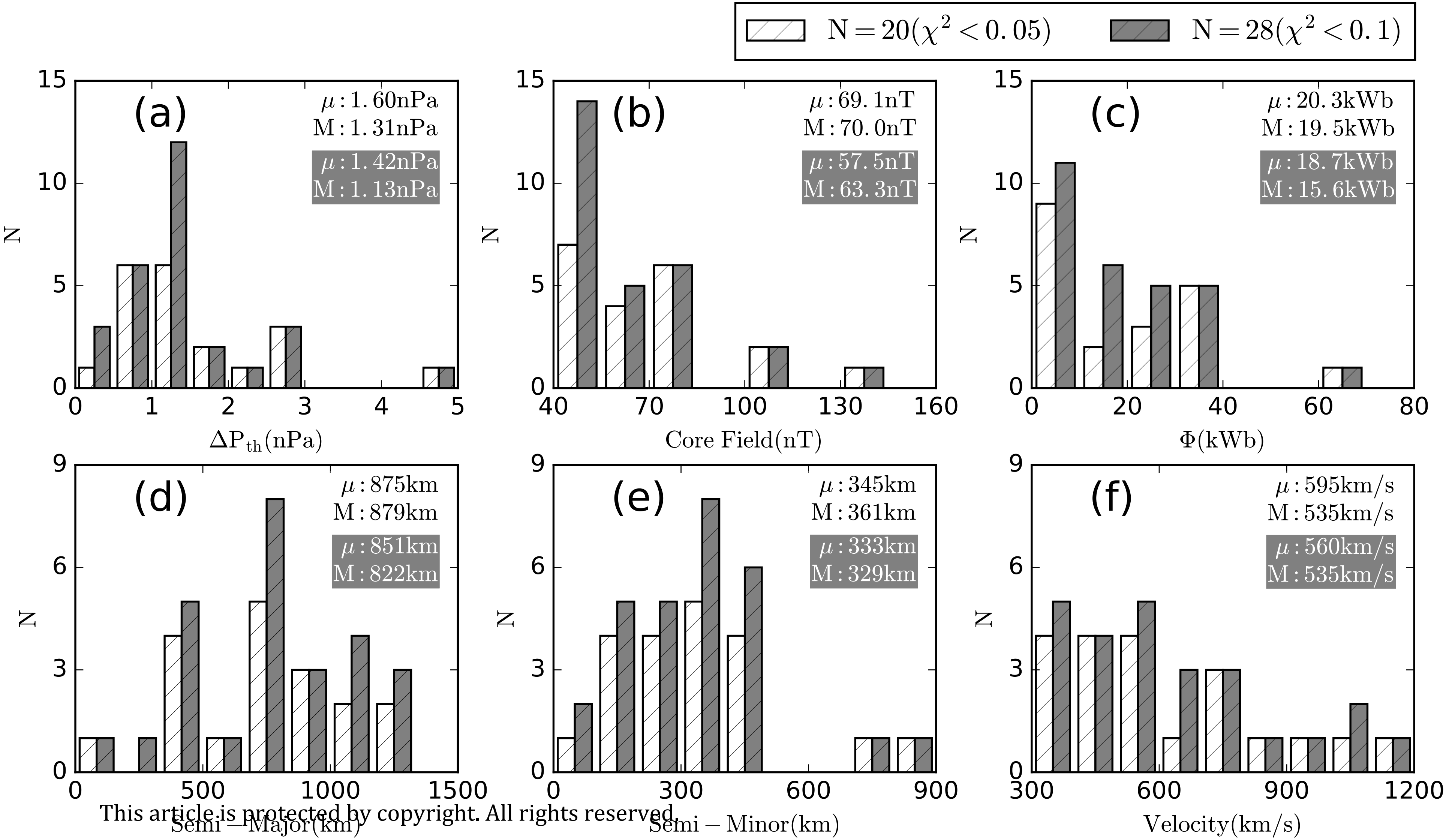
N = 20(χ² < 0.05)
N = 28(χ² < 0.1)
(a)
μ : 1.60nPa
M : 1.31nPa
μ : 1.42nPa
M : 1.13nPa
N
ΔP_th(nPa)
(b)
μ : 69.1nT
M : 70.0nT
μ : 57.5nT
M : 63.3nT
Core Field(nT)
(c)
μ : 20.3kWb
M : 19.5kWb
μ : 18.7kWb
M : 15.6kWb
Φ(kWb)
(d)
μ : 875km
M : 879km
μ : 851km
M : 822km
Semi − Major(km)
(e)
μ : 345km
M : 361km
μ : 333km
M : 329km
Semi − Minor(km)
(f)
μ : 595km/s
M : 535km/s
μ : 560km/s
M : 535km/s
Velocity(km/s)

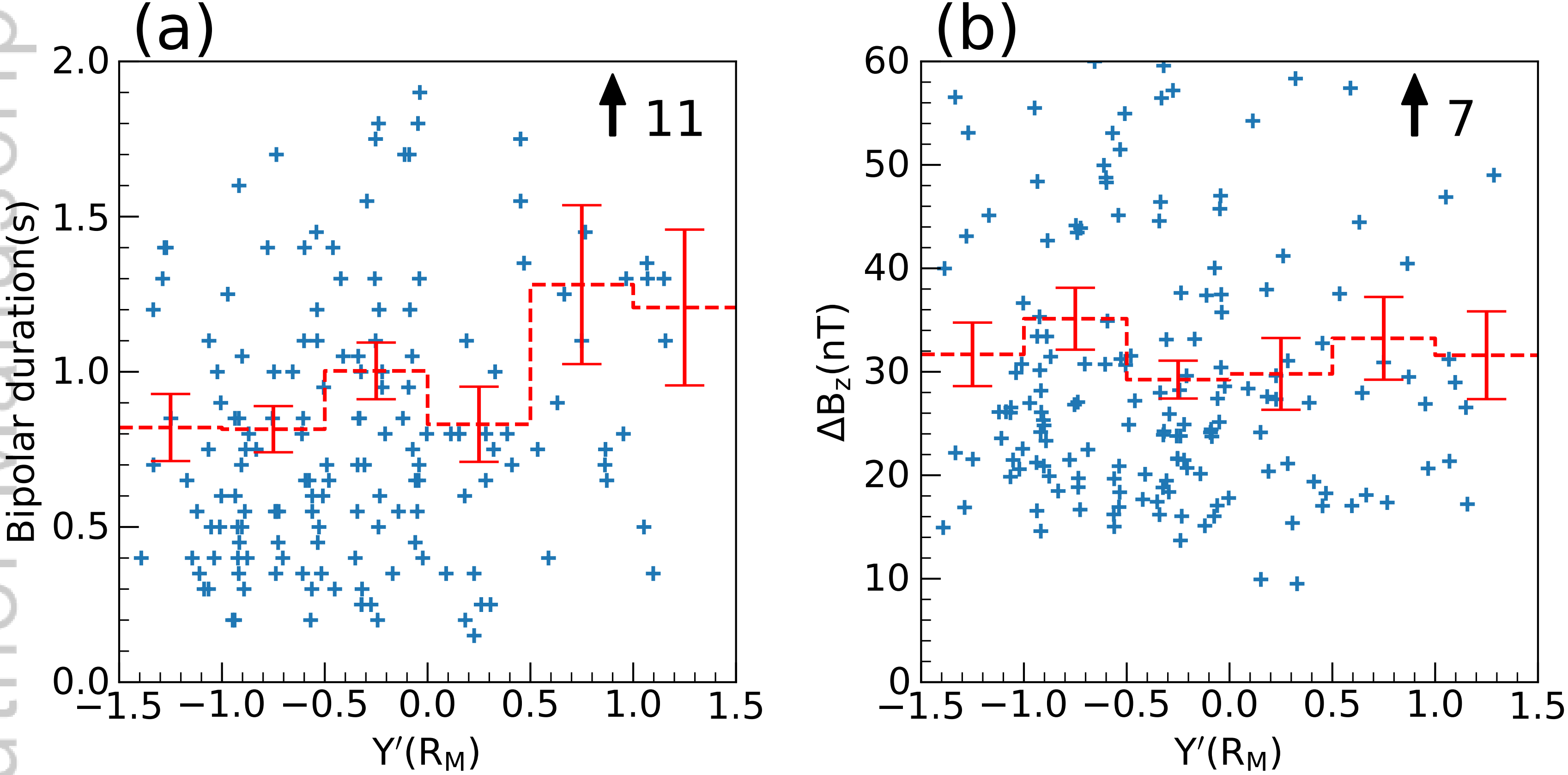

(a)
11
Bipolar duration(s)
0.0
0.5
1.0
1.5
2.0
−1.5
−1.0
−0.5
0.0
0.5
1.0
1.5
Y′(R_M)
(b)
7
ΔB_z(nT)
0
10
20
30
40
50
60
−1.5
−1.0
−0.5
0.0
0.5
1.0
1.5
Y′(R_M)